

Atomic spin coherence in superconducting microtraps

Dissertation

zur Erlangung des Grades eines Doktors
der Naturwissenschaften
der Fakultät für Mathematik und Physik
der Eberhard-Karls-Universität zu Tübingen
vorgelegt von

Brian Kasch

aus Milwaukee / U.S.A.

2010

Tag der mündlichen Prüfung: 21 Mai 2010

Dekan: Prof. Dr. Wolfgang Knapp

1. Berichterstatter: Prof. Dr. József Fortágh

2. Berichterstatter: Prof. Dr. Reinhold Kleiner

Contents

1	Introduction	1
2	Theoretical foundations	5
2.1	The Meissner effect in magnetic traps	5
2.1.1	London theory of superconductivity	5
2.1.2	Superconducting wire trap parameters	7
2.1.3	Trap depth	10
2.1.4	Hamiltonian of a magnetic dipole	11
2.2	Atomic spin coherence near surfaces	12
2.2.1	Spectral density of thermal magnetic field fluctuations	12
2.2.2	Maxwell's equation in Fourier space	13
2.2.3	Method of Green's functions	14
2.2.4	Field operators	15
2.2.5	Hamiltonian of a single atom interacting with an electromagnetic field	15
2.2.6	Calculation of the spectral density	15
2.2.7	Derivation of the spin-flip rate	16
2.2.8	Spin-flip rate near a normal conductor	17
2.2.9	Spin-flip rate near a super conductor	19
3	Experimental apparatus	21
3.1	Vacuum System	21
3.1.1	Vacuum Chamber	21
3.1.2	Vacuum Pumps	22
3.1.3	The road to UHV	24
3.1.4	Background pressure	25
3.2	BEC apparatus	25
3.2.1	In-vacuum setup	26
3.3	MOT overview	27
3.4	Laser system	28
3.4.1	Laser components	28
3.4.2	MOT light	29

3.4.3	Optical dipole trap and transfer	30
3.5	Cryogenic trap	32
3.5.1	Cryostat	33
3.5.2	Cryogenic wire trap	35
3.6	Imaging	36
3.7	Experimental timing	38
4	Measurements in the superconducting microtrap	41
4.1	Meissner effect	41
4.2	Spin coherence lifetime	44
4.2.1	Lifetime measurements	44
4.2.2	Niobium measurements	44
4.2.3	Niobium distance calibration	48
4.2.4	Copper measurements	48
4.2.5	Copper distance calibration	49
4.2.6	Trap lifetime: contributing factors	50
4.2.7	Surface evaporation	51
5	Conclusion	53
A	Computer control	57
A.1	ADwinControl	57
A.2	Experimental timing plots	59
A.3	Matlab	63
A.3.1	Magnetic field simulations	63
A.3.2	Automatic Adwin script generation	65
A.3.3	Data analysis GUI	69
B	Rubidium	73
B.1	Hyperfine structure	73

List of Figures

2.1	Meissner trap	8
2.2	Radial trap depth and frequency	11
2.3	Theoretical trap lifetime vs. surface distance above a normally conducting slab at various temperatures/offset fields	18
2.4	Skip depth vs. temperature for Cu and Nb	18
2.5	Theoretical lifetime near a superconductor	20
3.1	Inside setup photo / design	22
3.2	Vacuum schematic	23
3.3	Rf adding circuit	27
3.4	MOT diagram	29
3.5	Laser scheme	31
3.6	Nb wire superconducting transition	33
3.7	Thermal and electrical conductivities	35
3.8	cryostat cold finger photo / wire guide	36
3.9	ODT and Imaging scheme	37
4.1	Temperature dependence of the Meissner effect in the SCMT	42
4.2	Atom number and temperature vs. time in SCMT	45
4.3	Loss rate demonstrating absence of Johnson noise	47
4.4	Lifetime comparison	48
4.5	Copper lifetimes	49
4.6	Angle approach to copper	50
A.1	Experimental timing: Sisyphus, optical pumping, and magnetic trap	60
A.2	Experimental timing: magnetic transfer	61
A.3	Experimental timing: superconducting microtrap	62
A.4	Screen shot of yodaGUI	71
B.1	Rb hyperfine structure	74

Chapter 1

Introduction

Quantum theory is the most precise predictive tool known to man. The underlying formalism is nearly universal in scope, and has been used to explain phenomena from sub-nuclear to cosmic scales. Modern devices exploiting quantum physics are now ubiquitous. One need look no further than the modern computer. Hard drive read heads and transistors utilizing quantum effects have fueled a technological revolution, ironically, in classical computing. Classical computation has in turn brought insight into the quantum realm via approximate numerical methods, such as quantum Monte Carlo simulations. However, an exact calculation of a quantum many-body systems is untenable, even by the fastest supercomputers, since the full simulation of an N-body quantum system requires exponentially greater classical resources with increasing N (Nie00). In 1981, Feynman pointed out that quantum computers can handle certain problems, such as exact simulations of quantum many-body dynamics, more efficiently than classical computers (Fey82). Despite recent pioneering demonstrations of quantum calculations (Lan10), many challenges remain to the construction of a fully functional quantum computer.

Decoherence is one of the central obstacles to quantum computing (Zur03; Sho95). To minimize decoherence, it is advantageous to decouple a system from the influence of its environment. Trapped gasses of cold neutral atoms in vacuum have the advantage of being very weakly coupled to their environment. Furthermore, such systems are readily condensed into the ground state of their confining potential by a combination of laser and evaporative cooling. This makes them a potentially useful testbed in which to store quantum information. To make use of such a storage protocol requires that information be readily and coherently transferable to and from the atomic system. On this front, if an atomic cloud could be efficiently coupled to a solid state system, it would open up new avenues toward the realization of scalable devices for quantum computing (Sør04; Pet08; Sin09).

Since their inception, magnetic microtraps (atom chips) have proven a promising tool for the investigation of quantum gases. In 2001, two groups independently created a Bose-Einstein condensate (BEC) using lithographically patterned wires on a substrate (Ott01;

Hän01). Since then, many interesting experiments have been carried out, demonstrating for instance BEC diffraction from a magnetic lattice potential (Gün07), and tight one dimensional traps for quantum gases (Es09). These experiments utilize the key feature of atom chips, namely the ability to bring the atoms in close proximity to a conducting solid. In this way, larger gradients and higher trap frequencies can be realized. Traditionally the conducting wires of the atom chip are at room temperature or greater due to resistive heating. The question then naturally arises, to what extent does this surface influence the atomic cloud, nine orders of magnitude colder, and just microns away?

To investigate this question theoretically, Henkel et al. (Hen99) consider a magnetically trapped atom in the presence of an arbitrary linear (and local) dielectric half space. A magnetic atom can undergo spin flip transitions when subjected to magnetic field fluctuations at the Larmor frequency. Since only those atomic spin states whose Zeeman energy is minimized at the trap center experience a trapping potential, the coupling among Zeeman sublevels leads to atom loss. The authors identify the source of the fluctuating magnetic field as emanating from microscopic electrical current fluctuations (Johnson noise) within the solid, which are intrinsic to any resistive material. Furthermore, they derive a scaling law for the expected decay rate of an atomic cloud as a function of its distance from the surface. This decay rate, which is (trivially) inversely related to the trap lifetime, has been measured in atom chip systems utilizing normally conducting wires (Har03; Jon03).

These measurements highlight a significant limitation when approaching within $100\ \mu\text{m}$ of a metallic surface at room temperature. Here the lifetime was observed to drop below the background value of 120 s, to less than 5 s at $20\ \mu\text{m}$, in good quantitative agreement with theoretical models.

It was noted that superconductors offer a particularly elegant way to circumvent the deleterious effects of Johnson noise. In an ideal superconductor, dissipation is absent. In accordance with the fluctuation-dissipation theorem, the problematic magnetic field fluctuations vanish. Theoretical accounts considering atom-chip style geometries show that the corresponding lifetime (after taking into account finite temperature effects) is expected to be orders of magnitude greater near an ideal superconductor than near a normal conductor (Sch05; Ska06; Hoh07). What is more, cryogenically cooled atom chips enable the integration of superconducting devices, such as Josephson junctions, and SQUIDs.

This led our group and two others to construct first generation cryogenic microtrap systems. The group of S. Haroche has created the first BEC on a superconducting atom chip (Rou08), and subsequently measured the cloud lifetime in the normal conducting region of their atom chip (Emm09). Their results for the lifetime near copper are consistent with our own. In particular, an increase of the lifetime was observed near the low temperature normal metal, but was still limited by Johnson noise. The group of Shimizu built an atom trap formed of a closed superconducting loop (Muk07), and has subsequently investigated vortices in superconducting thin films (Huf09; Shi09).

We have built an experiment capable of trapping ultracold atoms as close as $20\ \mu\text{m}$

from a superconducting surface. The setup combines a room temperature BEC apparatus with a separate, niobium-wire trap mounted on a thermally shielded helium flow cryostat. Atoms are transported via magnetic and optical fields into the cryogenically cooled superconducting microtrap, where we have measured the Meissner effect of the wire on the trap position (Can08a), and the lifetime of trapped atoms as a function of surface distance (Kas10). The latter measurements demonstrate that superconductors can lead to trapping lifetimes which exceed the Johnson noise limit for normal metals at cryogenic temperatures. This is the central result of this thesis.

The result points the way towards atom chip devices in which the long lived spin coherence of atomic clouds at micron distances from the surface is essential. Such devices are important for proposals aimed at realizing the coupling of atomic samples to solid state structures.

This thesis is laid out as follows: in chapter 2 the theory behind the Meissner effect in superconducting microtraps is presented, and additionally, the spin flip rate for clouds trapped near normal metals is derived. This allows us to estimate the expected lifetime near cold copper, which acts as our reference material. Ch. 3 details the experimental setup. In Ch. 4, we present the measurement results, demonstrating the absence of Johnson noise from a superconductor to within our experimental sensitivity. Finally, in Ch. 5, we conclude with an outlook toward promising future experiments with ultracold atoms in cryogenic environments. Appendix A gives details of the experimental computer control, and Appendix B shows the hyperfine spectrum of rubidium, the atomic species used for our experiments.

Chapter 2

Theoretical foundations

This chapter contains two sections. In the first, I will present the London theory of superconductivity, and use it to calculate the properties of a magnetic trap near a cylindrical wire in the Meissner state. The second section is concerned with deriving the spin-flip rate for an atomic cloud trapped near a conducting surface. The resulting expression may be applied to calculate the expected lifetime of an ultracold cloud as a function of its separation from the surface of a normal, or superconductor.

2.1 The Meissner effect in magnetic traps

This section shows how the London theory of superconductivity, which dictates the exclusion of magnetic fields at a superconductor surface within the London penetration depth, effects the properties of a nearby magnetic trap. Analytical expressions for the position, gradient, trap frequency, and trap depth are found.

2.1.1 London theory of superconductivity

The first observation of superconductivity came nearly a century ago, when in 1911, Kamerlingh Onnes and coworkers at the University of Leiden measured the vanishing resistance of mercury below 4.2K. It was not until 1933 that Meissner and Ochsenfeld demonstrated experimentally the expulsion of static magnetic fields from the region within a superconductor. The brothers Fritz and Heinz London subsequently provided a phenomenological description of superconductivity that successfully explained the Meissner-Ochsenfeld effect.

The London equations for the magnetic and electric fields produced by a supercurrent, \mathbf{J}_s , are (Buc04)

$$\nabla \times \mathbf{J}_s = -\frac{1}{\mu_0 \lambda_L^2} \mathbf{B} \quad (2.1)$$

$$\frac{\partial \mathbf{J}_s}{\partial t} = \frac{1}{\mu_0 \lambda_L^2} \mathbf{E} \quad (2.2)$$

where the London penetration depth, defined as

$$\lambda_L = \sqrt{\frac{m}{n_s e^2 \mu_0}} \quad (2.3)$$

describes the characteristic length scale over which the magnetic field exponentially decays within an ideal superconductor. Here m is the electron mass, e is the elementary charge, and n_s is the density of superconducting electrons. In the London theory, the number density of superconducting electrons as a function of temperature is

$$n_s(T) = n_0 \left(1 - \left(\frac{T}{T_c} \right)^4 \right) \quad (2.4)$$

This quantity rapidly approaches zero near the transition temperature, whereas at $T = 0$, all n_0 electrons are superconducting.

The London theory provides no insight into the mechanism behind superconductivity. By 1938, in another landmark publication (Lon38), F. London proposed a description of superfluidity in He II relying on the concept of macroscopic occupation of the energetic ground state, Bose-Einstein condensation. Although appealing, it was not clear how this concept could apply to a fermi sea of electrons in a metal. In 1946, R. Ogg put forward the idea that superconductivity results from the condensation of spatially separate, localized electron pairs (Ale03). This idea did not take hold, since it did not account for experimental measurements. In 1957, L. Cooper showed that electrons, which couple to the background ionic lattice, could form an attractive interaction via the exchange of virtual phonons, thereby lowering their energy with respect to the fermi sea. In this formulation, electrons of equal and opposite momentum form pairs, with a high degree of spatial overlap. The superconducting ground state forms, consisting of a macroscopic occupation of cooper-paired electrons.

Before the microscopic pairing mechanism was understood, Ginzburg and Landau made a crucial contribution to the understanding of superconductivity by postulating the existence of an order parameter to describe the superconducting state Ψ (Gin50). By expanding in powers of Ψ , they elucidated the thermodynamics of the superconducting state. This theory was used e.g. to show that vortices in a mixed-state type II superconductor arrange in a regular triangular array (Ess67), the so called Abrikosov lattice. The size of a vortex core is typically of the order ξ_0 , i.e. the coherence length introduced by Pippard to account for experimental variations of the London penetration depth due to non-local effects (Pip53).

With the invention of BCS theory (Bar57), low temperature superconductivity has been described at the microscopic level. The theory has been highly successful in this regime in predicting quantities such as the magnitude of the energy gap. In many simple cases BCS theory dictates only a small perturbation to quantities calculated via the Ginzburg-Landau or London theories. In fact Gor'kov showed the Ginzburg-Landau theory can be viewed as a limiting case of the BCS theory at temperatures near T_c with no external magnetic field.

BCS theory is directly applicable to superconductors that exhibit s-wave symmetry in the energy gap (described by the order parameter). For high temperature superconductors, extensions of Eliashberg theory have been used that take into account the observed d-wave symmetry of the energy gap (Sch03). Despite this considerable series of advancements, the microscopic mechanism behind high temperature superconductors remains unknown.

2.1.2 Superconducting wire trap parameters

Let us consider a straight (infinitely long) cylindrical superconducting wire of radius R carrying a current I . With $I = 0$, we apply a constant external bias field B_x along x . The Meissner effect leads to the complete exclusion of magnetic fields from the interior of a superconductor by generating screening currents in the wire. An inhomogeneous total bias field B_b results. In cylindrical coordinates, the field has components (Dik09),

$$B_r = B_x \left(1 - \left(\frac{R^2}{\rho^2} \right) \right) \sin \theta \quad (2.5)$$

$$B_\theta = B_x \left(1 + \left(\frac{R^2}{\rho^2} \right) \right) \cos \theta \quad (2.6)$$

where ρ is the distance from the wire center, and θ is the angle with the z -axis. Qualitatively, circulating currents within a thin surface layer exactly cancel the externally applied field just inside the surface. Fields parallel to the surface plane can jump to a finite value discontinuously at the surface boundary, whereas orthogonal fields cannot. The magnetic field has two zeros at the surface boundary, precisely where the parallel fields vanish.

Now imagine we slowly increase the wire current from zero. The resulting magnetic field magnitude as a function of the distance, z , from the wire center, is given by the usual expression

$$B_I = \frac{\mu_0 I}{2\pi z} \quad (2.7)$$

For small currents, the wire field is not able to cancel the bias field. However, the locations of the zeros on opposite sides of the wire surface are shifted symmetrically toward the bottom of the wire. At the same time, a saddle point approaches from infinity, forming a local minimum along z at

$$z_{sp} = \frac{\mu_0 B_x R^2}{4\pi I} \quad (2.8)$$

and a local maximum along x . As the wire field is further increased, the surface zeros travel toward the each other along quarter-circular paths, eventually merging with each other (and the approaching saddle point) at the wire surface where $x = 0$. Further increasing the wire field leads to a cancelation of the bias field away from the wire surface, i.e. a magnetic quadrupole minimum suitable for trapping atoms. Fig. 2.1 shows contours of the total field magnitude, starting at $I = 0$ (2.1a). At intermediate fields (2.1b and c), the saddle point is seen to approach the wire surface. Finally, at sufficiently high current (2.1d), a magnetic quadrupole minimum appears and moves away from the surface.

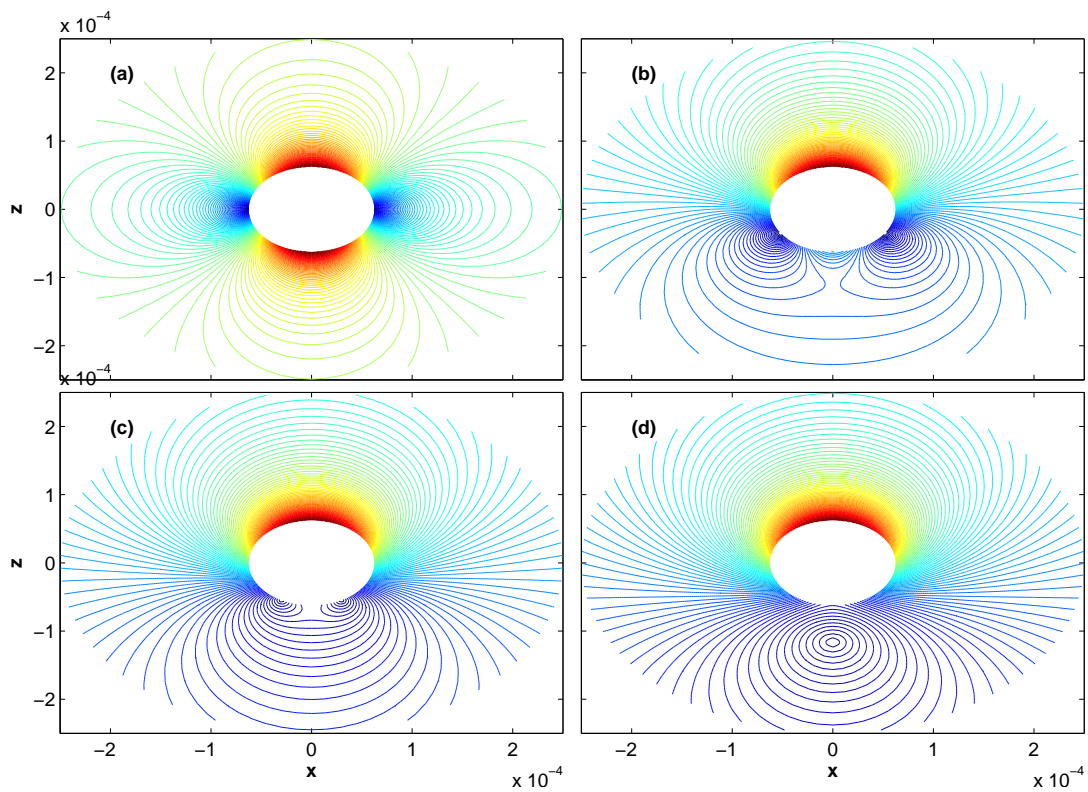


Figure 2.1: Contour plots of the magnetic field magnitude for four different values of wire current. The external bias field is 20 G in all plots, and the wire current is: (a) $I = 0$ A, (b) $I = 0.7$ A, (c) $I = 1.1$ A, (d) $I = 1.5$ A

2.1. The Meissner effect in magnetic traps

We now restrict our attention to the field along the z -axis, where the bias field points purely in the x -direction,

$$B_b = B_x \left(1 + \left(\frac{R}{z} \right)^2 \right) \quad (2.9)$$

The field equals $2B_x$ at the surface, $z = R$, with no current in the wire. Conversely the field approaches B_x in the limit $x \rightarrow \infty$. The inhomogeneity introduced onto the bias field by the deformation of the field lines around the wire adds an additional term to the field gradient. At the trap minimum, $z_{0,SC}$, we have,

$$a_{0,SC} = \frac{B_x}{z_{0,SC}} \left(\frac{z_{0,NC}}{z_{0,SC}} - 2 \left(\frac{R}{z_{0,SC}} \right)^2 \right) \quad (2.10)$$

Using the equality

$$\frac{z_{0,NC}}{z_{0,SC}} = 1 + \left(\frac{R}{z_{0,SC}} \right)^2 \quad (2.11)$$

this reduces to

$$a_{0,SC} = \frac{B_x}{z_{0,SC}} \left(1 - \left(\frac{R}{z_{0,SC}} \right)^2 \right) \quad (2.12)$$

Table 2.1 provides a comparison of trap properties for normal and superconducting wires.

Table 2.1: Some key properties of normal and superconducting traps.

Trap feature	Normal conducting (NC)	Superconducting (SC)
Minimum (z_0)	$\frac{\mu_0 I}{2\pi B_x}$	$\frac{\mu_0 I}{4\pi B_x} + \sqrt{\left(\frac{\mu_0 I}{4\pi B_x} \right)^2 - R^2}$
Gradient (a_0)	$-\frac{2\pi B_x^2}{\mu_0 I}$	$\frac{B_x}{z_{0,SC}} \left(1 - \left(\frac{R}{z_{0,SC}} \right)^2 \right)$
Depth ($B_{\Delta'}$)	$B_x - \frac{\mu_0 I}{2\pi R}$	$\left(B_x - \frac{\mu_0 I}{2\pi R} \right) + \frac{1}{4B_x} \left(\frac{\mu_0 I}{2\pi R} \right)^2$

We now show the expression for the curvature of the field along z ,

$$\frac{d^2 B}{dz^2} = \frac{6B_x R^2}{z^4} - \frac{\mu_0 I}{\pi z^3} \quad (2.13)$$

which can be used to calculate the theoretical frequency in the z direction from,

$$\omega_z = \frac{1}{2\pi} \left\{ \frac{1}{m_{Rb}} \left(-m_{FGF} \mu_B \frac{d^2 B}{dz^2} \Big|_{z=z_0} \right) \right\} \quad (2.14)$$

Unlike in the normal conducting case, the trap curvature has a local maximum as we approach the wire by reducing the current. The distance z^* at which the trap frequency

is maximized can be calculated by setting the derivative of the curvature to zero. The maximum trap frequency occurs at a distance

$$z^* = \sqrt{3}R \quad (2.15)$$

from the wire center.

2.1.3 Trap depth

To calculate the depth $B_{\Delta,SC}$ of a superconducting wire trap, we consider the fields at the wire surface, and very far from the wire. Whichever of these two quantities is smaller limits the magnetic field trap depth. The two possibilities are,

$$\begin{aligned} B_{\Delta'',SC} &= B_x && \text{if } I > \frac{2\pi R B_x}{\mu_0} \text{ (Far)} \\ B_{\Delta',SC} &= (B_b - B_I)|_{x=R} && \text{if } I < \frac{2\pi R B_x}{\mu_0} \text{ (Close)} \end{aligned}$$

Here the double/single prime denotes a trap formed far/close to the wire surface, respectively. For a superconductor, the trap depth is limited by the wire surface when $I < 2\pi R B_x / \mu_0$. Interestingly, this condition is exactly reversed for a normal conductor, in which case the surface field is smaller than the external bias when $I > 2\pi R B_x / \mu_0$. Far from the wire, the superconducting trap depth is simply B_x . In practice, the trap depth is reduced by gravity, which introduces a potential gradient equivalent to ≈ 15 Gauss/cm.

The optimal trap depth occurs when $B_x = (B_b - B_I)|_{x=R}$ or $I = 2\pi R B_x / \mu_0$. In this case,

$$B_{\Delta^*,SC} = \frac{1}{4} \left(\frac{\mu_0 I}{2\pi R} \right) \quad (2.16)$$

Close to the wire (i.e. $B_x < \mu_0 I / 2\pi R$), the trap opens toward the surface and the expression becomes,

$$B_{\Delta',SC} = \left(B_x - \frac{\mu_0 I}{2\pi R} \right) + \frac{1}{4B_x} \left(\frac{\mu_0 I}{2\pi R} \right)^2 \quad (2.17)$$

Because the first and second terms have opposite sign, there is a reduction of the trap depth by

$$\frac{1}{4B_x} \left(\frac{\mu_0 I}{2\pi R} \right)^2 \quad (2.18)$$

with respect to a normal conducting trap which has a maximum trap depth close to the wire (when there is no offset field) of

$$B_{\Delta',NC} = B_x - \frac{\mu_0 I}{2\pi R} \quad (2.19)$$

Introducing a homogeneous offset field (along the y-axis) reduces the trap depth. The Meissner effect, however, plays only a minor role since the demagnetization factor in this direction is negligible (Can08b).

Fig. 2.2 shows the trap depth (a), and the analytical radial trap frequency (b) for a superconducting wire trap with experimentally realistic parameters.

The trap depth falls with decreasing cloud-surface distance as d^2 from an energy of $\approx k_B \times 25 \mu\text{K}$ at $50 \mu\text{m}$ to less than $k_B \times 2 \mu\text{K}$ at $20 \mu\text{m}$.

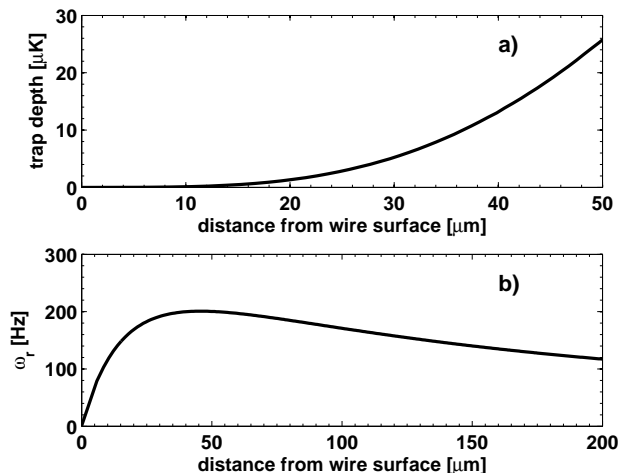


Figure 2.2: The trap depth (a), and radial frequency (b) calculated from Eq. 2.17 and Eqs. 2.14, 2.13, respectively. The maximum trap frequency occurs at $z^* = \sqrt{3}R$. The trap depth falls to zero sub-linearly at the trap surface in contrast to a normally conducting trap.

2.1.4 Hamiltonian of a magnetic dipole

We now consider the interaction of an atom with an inhomogeneous magnetic field, such as a magnetic trap. The atom carries a magnetic dipole moment $\boldsymbol{\mu}$, which in the presence of a field \mathbf{B} has magnetic potential energy given by the Zeeman Hamiltonian,

$$H_Z = -\boldsymbol{\mu} \cdot \mathbf{B} \quad (2.20)$$

$$= -m_F g_F \mu_B |B| \quad (2.21)$$

where the second line arises in cases where the atomic magnetic moment can smoothly follow the changing magnetic field. More precisely, the atom retains its magnetic substate so long as the adiabatic condition, expressed as $d\omega_L/dt \ll \omega_L^2$, is fulfilled. Here we have introduced the Larmor frequency,

$$\omega_L = g_F \mu_B |B| / \hbar \quad (2.22)$$

which in the classical case is simply the precession frequency of the magnetic moment about the axis of a homogeneous field. A photon at the Larmor frequency can induce an atomic "spin-flip" transition between two neighboring Zeeman substates.

The Lande factor, g_F , describes the ratio of the magnetic moment and the angular momentum quantum number. Both the electronic (spin-orbital) and nuclear g-factors contribute to g_F .

$$g_F = g_J \frac{F(F+1) + J(J+1) - I(I+1)}{2F(F+1)} - g_I \frac{\mu_N}{\mu_B} \frac{F(F+1) + I(I+1) - J(J+1)}{2F(F+1)} \quad (2.23)$$

where $\mu_N = e\hbar/2m_p$ is the nuclear magnetic moment. For rubidium in its ground state $g_F \approx -1/2$ to within 1 part in 1000 (approximately the ratio of the electron and proton

masses). The difference from $1/2$ arises from the contribution of the nuclear magnetic moment, as well as the anomalous g_S factor of the electron spin. For an atom trapped in the hyperfine state $m_F = 2$, the minimum potential energy occurs in regions of weakest field. Such atoms are thus referred to as "weak-field seekers".

2.2 Atomic spin coherence near surfaces

In this section, we seek the expression for the electromagnetic fields emanating from an electrical conductor with fluctuating currents resulting from finite temperature and resistance. This has been a subject of considerable interest, with broad applicability in quantum and atom optics. We follow the general theoretical framework laid out by Vogel and Welsch (Vog06), Scheel and coworkers (Sch98; Sch99), and earlier by Agarwal (Aga75a; Aga75b). Henkel et al. (Hen99; Hen05), and Rekdal et al. (Rek04) derive the atomic spin flip rate for a cloud trapped near dielectric matter in a half plane, and two-layered wire configuration respectively. Scheel et al. (Sch05) first extended the analysis to include superconducting structures, a topic which was further elaborated upon by Hohenester et al. (Ska06).

2.2.1 Spectral density of thermal magnetic field fluctuations

We consider a local, linear dielectric¹ medium. The material's response to external fields is represented by its electric permittivity, with ϵ_0 denoting the vacuum permittivity. The permittivity is related to the electric susceptibility by

$$\epsilon(\mathbf{r}, \omega) = 1 + \int_0^\infty d\tau e^{i\omega\tau} \chi(\mathbf{r}, \tau) \quad (2.24)$$

where the latter term is the fourier transform (FT) of the time dependent susceptibility, yielding an expression in the frequency domain. Inhomogeneities are accounted for by the spatial and frequency dependence of $\epsilon(\mathbf{r}, \omega)$, which has both real and imaginary parts corresponding to dispersion and absorption respectively. Causality dictates that the permittivity satisfies the Kramers-Kronig relations (Dun98).

Details regarding the specific composition and geometry of the dielectric make their way into the Green tensor, which (with the appropriate boundary conditions) uniquely solves the inhomogeneous Helmholtz equation with δ -function driving term. The noise process within the material is described by introducing a noise polarization (or current), whose operators necessarily satisfy the equal-time commutation relations (Sch98). Dissipation resulting from the finite resistance implies current fluctuations in accordance with the fluctuation-dissipation theorem.

¹Although the term "dielectric" typically refers to semiconducting materials, here we use the term to denote any material with finite electric polarizability, including metals.

Exterior to the surface, the field fluctuations arise essentially from the material's near-field blackbody radiation (i.e. δ -correlated noise following Bose-Einstein statistics). Electromagnetic screening damps interior fluctuations on the length scale of the skin depth, defined as

$$\delta = \sqrt{2/\omega\mu_0\sigma(T)} \quad (2.25)$$

It is the material within one skin depth of the surface that largely determines the noise properties at the location of the trapped atoms. Fluctuations of the magnetic field at the Larmor frequency ($\omega = \omega_L$) directly out-couple atoms from the magnetic trap by the spin-flip chain $|F = 2, m_F = 2 \rangle \rightarrow |F = 2, m_F = 1 \rangle \rightarrow |F = 2, m_F = 0 \rangle$. We shall now derive an expression for the spectral density of the magnetic field noise in terms of the Green tensor (Eq. 2.51), from which specific (geometry dependent) loss rates can be calculated.

2.2.2 Maxwell's equation in Fourier space

Let us begin at the starting point of most arguments of electromagnetic theory. Maxwell's equations in the presence of dielectric matter (in SI units) can be written

$$\nabla \cdot \mathbf{B} = 0 \quad (2.26)$$

$$\nabla \times \mathbf{E} + \frac{\partial}{\partial t} \mathbf{B} = 0 \quad (2.27)$$

$$\nabla \cdot \mathbf{D} = \rho_f \quad (2.28)$$

$$\nabla \times \mathbf{H} - \frac{\partial}{\partial t} \mathbf{D} = \mathbf{J}_f \quad (2.29)$$

where $\mathbf{D} = \epsilon_0 \mathbf{E} + \mathbf{P}$, and $\mathbf{H} = \frac{1}{\mu_0} \mathbf{B} - \mathbf{M}$ for linear media. We restrict our attention to non-magnetic materials ($\mathbf{M} = 0$). Furthermore we focus on the source-free case $\rho_f = 0$, $\mathbf{J}_f = 0$, since we are primarily concerned with field fluctuations.

We proceed by taking the FT of the above equations, from which we obtain the corresponding equations in the frequency domain (Gru96). Upon rearranging,

$$\nabla \cdot \mathbf{B}(\mathbf{r}, \omega) = 0 \quad (2.30)$$

$$\nabla \times \mathbf{E}(\mathbf{r}, \omega) = i\omega \mathbf{B}(\mathbf{r}, \omega) \quad (2.31)$$

$$\epsilon_0 \nabla \cdot (\epsilon(\mathbf{r}, \omega) \mathbf{E}(\mathbf{r}, \omega)) = -\nabla \cdot \mathbf{P}_N(\mathbf{r}, \omega) \quad (2.32)$$

$$\nabla \times \mathbf{B}(\mathbf{r}, \omega) + \frac{i\omega}{c^2} \epsilon(\mathbf{r}, \omega) \mathbf{E}(\mathbf{r}, \omega) = -i\omega \mu_0 \mathbf{P}_N(\mathbf{r}, \omega) \quad (2.33)$$

where we have inserted an expression for the electric displacement,

$$\mathbf{D}(\mathbf{r}, \omega) = \epsilon_0 \epsilon(\mathbf{r}, \omega) \mathbf{E}(\mathbf{r}, \omega) + \mathbf{P}_N(\mathbf{r}, \omega) \quad (2.34)$$

The noise polarization $\mathbf{P}_N(\mathbf{r}, \omega)$ plays the role of a local source term for spontaneous fluctuations of the electric field within the medium. To determine the electric field we

plug Eq. 2.31 into 2.33 and multiply through by $i\omega$ to find

$$\nabla \times \nabla \times \mathbf{E}(\mathbf{r}, \omega) - \frac{\omega^2}{c^2} \epsilon(\mathbf{r}, \omega) \mathbf{E}(\mathbf{r}, \omega) = \omega^2 \mu_0 \mathbf{P}_N(\mathbf{r}, \omega) \quad (2.35)$$

This is a generalized form of the inhomogeneous Helmholtz wave equation. In cases where the charge distribution is homogeneous it reduces to the standard Helmholtz equation via the vector identity $\nabla \times \nabla \times \mathbf{E} = \nabla(\nabla \cdot \mathbf{E}) - \nabla^2 \mathbf{E}$.

2.2.3 Method of Green's functions

Equation 2.35 can be solved using the powerful methods of Green's functions. For a rigorous treatment of Green's functions, see e.g. Ref. (Byr92). An excellent short introduction set in a historical context is given in Ref. (Cha03). The basic idea is as follows: for a linear differential operator L (in \mathbb{R}^3), we seek the solutions of $u(\mathbf{r})$ satisfying

$$Lu(\mathbf{r}) = f(\mathbf{r}) \quad (2.36)$$

where $f(\mathbf{r})$ represents an arbitrary driving term. Inverting this equation yields

$$u(\mathbf{r}) = L^{-1}f(\mathbf{r}) \equiv Kf(\mathbf{r}) \quad (2.37)$$

Clearly K has properties of an integral operator (being the inverse of a differential operator). The solutions of $u(\mathbf{r})$ are written

$$u(\mathbf{r}) = \int d\mathbf{r}' G(\mathbf{r}, \mathbf{r}') \cdot f(\mathbf{r}') \quad (2.38)$$

where we have used the Green function, defined via the relation

$$LG(\mathbf{r}, \mathbf{r}') = \delta(\mathbf{r} - \mathbf{r}') \quad (2.39)$$

The Green function determines the field at \mathbf{r} due to a point source at \mathbf{r}' , or arbitrary arrangement of such sources. To arrive at a unique solution for $G(\mathbf{r}, \mathbf{r}')$ (and likewise for $u(\mathbf{r})$) we must specify the boundary conditions. In free space we have that $G(\mathbf{r}, \mathbf{r}') \rightarrow 0$ as $r \rightarrow \infty$. At the interface of a metal with the vacuum, the simplest boundary conditions keep the magnetic and electric fields continuous. The normal component of the electric field goes to zero at the surface, however surface currents lead to a magnetic field jump across the interface.

From the above arguments, we now make the following correspondences for a given frequency ω : L is the linear (generalized) Helmholtz operator, $u(\mathbf{r}) \rightarrow \mathbf{E}(\mathbf{r}, \omega)$, $G(\mathbf{r}, \mathbf{r}') \rightarrow \mathbf{G}(\mathbf{r}, \mathbf{r}', \omega)$, and $f(\mathbf{r}) \rightarrow \mathbf{P}_N(\mathbf{r}, \omega)$.

Applying Eq. 2.39 to our problem, the Green tensor is seen to satisfy the equation

$$\nabla \times \nabla \times \mathbf{G}(\mathbf{r}, \mathbf{r}', \omega) - \frac{\omega^2}{c^2} \epsilon(\mathbf{r}, \omega) \mathbf{G}(\mathbf{r}, \mathbf{r}', \omega) = \delta(\mathbf{r} - \mathbf{r}') \mathbf{U} \quad (2.40)$$

where \mathbf{U} is the identity dyadic tensor.

2.2.4 Field operators

From Eq. 2.38, the electric field is given by

$$\mathbf{E}(\mathbf{r}, \omega) = \omega^2 \mu_0 \int d^3 r' \mathbf{G}(\mathbf{r}, \mathbf{r}', \omega) \cdot \mathbf{P}_N(\mathbf{r}', \omega) \quad (2.41)$$

According to Eq. 2.31, the magnetic field is given by

$$\mathbf{B}(\mathbf{r}, \omega) = \frac{1}{i\omega} \nabla \times \mathbf{E}(\mathbf{r}, \omega) \quad (2.42)$$

The noise term for the polarization density, \mathbf{P}_N , can be constructed from the elementary excitations as

$$\hat{\mathbf{P}}_N(\mathbf{r}, \omega) = i \sqrt{\frac{\hbar \epsilon_0}{\pi}} \epsilon_I \hat{\mathbf{f}}(\mathbf{r}, \omega) \quad (2.43)$$

The fundamental field operators have been chosen to be consistent with the fluctuation-dissipation theorem, and they satisfy the equal time commutation relations. The time evolution of the fundamental field operators $\hat{\mathbf{f}}(\mathbf{r}, \omega)$ (and h.c.) can be deduced by solving the Heisenberg equations of motion.

From the fundamental field operators, the electric and magnetic field operators can be obtained by plugging into the equations 2.43, 2.41, and 2.42.

2.2.5 Hamiltonian of a single atom interacting with an electromagnetic field

The Hamiltonian for a system composed of a single two level atom interacting with the electromagnetic field in the electric-dipole and rotating-wave approximations is given by (Vog06),

$$\hat{H} = \hat{H}_F + \hat{H}_{Int} \quad (2.44)$$

$$= \int d^3 \mathbf{r} \int_0^\infty d\omega \hbar \omega \hat{\mathbf{f}}^\dagger(\mathbf{r}, \omega) \hat{\mathbf{f}}(\mathbf{r}, \omega) \quad (2.45)$$

$$-i \sqrt{\frac{\hbar}{\pi \epsilon_0}} \int_0^\infty d\omega \frac{\omega^2}{c^2} \int d^3 r' \mathbf{d}_{21} \mathbf{G}(\mathbf{r}, \mathbf{r}', \omega) \hat{\mathbf{f}}(\mathbf{r}', \omega) \hat{A}_{21} \quad (2.46)$$

Where $\hat{A}_{21} = |2\rangle\langle 1|$, and $\mathbf{d}_{21} = \langle 2|\hat{\mathbf{d}}|1\rangle$ is the dipole operator matrix element between the states $|1\rangle$ and $|2\rangle$.

2.2.6 Calculation of the spectral density

The field excitation spectrum is calculated by forming a correlation function of the field operators (Fer06),

$$\langle \hat{\mathbf{f}}_\alpha(\mathbf{r}, \omega) \hat{\mathbf{f}}_\beta^\dagger(\mathbf{r}', \omega') \rangle = (\bar{n}_{th} + 1) \delta_{\alpha\beta} \delta(r - r') \delta(\omega - \omega') \mathbf{U} \quad (2.47)$$

where α and β represent cartesian coordinates. At $T = 0$, the noise is strictly delta-correlated, arising from zero-temperature spontaneous vacuum fluctuations, whereas at

finite temperatures it includes a component proportional to the mean thermal photon occupation number, \bar{n}_{th} . The familiar result from Bose-Einstein statistics is

$$\bar{n}_{th} = \frac{1}{e^{\hbar\omega/k_B T} - 1} \quad (2.48)$$

Ultimately we are concerned with the spectral density of the magnetic field fluctuations at the Larmor frequency, which according to the Wiener-Khinchin theorem is given by the Fourier transform of the auto-correlation function,

$$S_B^{\alpha\beta}(\mathbf{r}, \mathbf{r}'; \omega_L) = \int_{-\infty}^{\infty} d\tau \langle B_\alpha(\mathbf{r}, t + \tau) B_\beta(\mathbf{r}', t) \rangle e^{i\omega_L \tau} \quad (2.49)$$

From the properties of the FT,

$$S_B^{\alpha\beta}(\mathbf{r}, \mathbf{r}'; \omega, \omega') = 2\pi\delta(\omega - \omega') \langle B_\alpha(\mathbf{r}, \omega) B_\beta(\mathbf{r}', \omega') \rangle \quad (2.50)$$

Invoking the fluctuation-dissipation theorem, the spectral density can also be expressed in terms of the Green tensor as

$$S_B^{\alpha\beta}(\mathbf{r}, \mathbf{r}'; \omega, \omega') = 2\hbar\mu_0(\bar{n}_{th} + 1)\delta(\omega - \omega') \text{Im}[\nabla \times \nabla' \times \mathbf{G}(\mathbf{r}, \mathbf{r}', \omega)]_{\alpha\beta} \quad (2.51)$$

2.2.7 Derivation of the spin-flip rate

Let us now consider an atomic cloud, magnetically trapped in the ground state at position \mathbf{r}_A near a finite temperature dielectric. For a Ioffe-type trap, magnetic fields at the Larmor frequency (ω_L from Eq. 2.22) lead to stimulated emission by the atoms on the transition $|F, m_F\rangle = |2, 2\rangle \rightarrow |2, 1\rangle$, and likewise $|2, 1\rangle \rightarrow |2, 0\rangle$. Whereas atoms in the $|2, 1\rangle$ state experience 1/2 the trapping potential, $|2, 0\rangle$ are not trapped. In this way, spin-flips usually correspond to loss from the magnetic trap.

The transition rate between the Zeeman substates ($|i\rangle \rightarrow |f\rangle$) on the atomic hyperfine manifold can be calculated via Fermi's golden rule (For07).

$$\Gamma^B(\mathbf{r}_A, \omega_L) = \sum_{\alpha, \beta=x,y,z} \frac{\langle f | \hat{\mu}_\alpha | i \rangle \langle i | \hat{\mu}_\beta | f \rangle}{\hbar^2} S_B^{\alpha\beta}(\mathbf{r}_A; \omega_L) \quad (2.52)$$

Expressed in terms of the Green tensor, this becomes

$$\Gamma^B(\mathbf{r}_A, \omega_L) = \mu_0 \frac{2(\mu_B g_F)^2}{\hbar} (\bar{n}_{th} + 1) \sum_{\alpha, \beta=x,y,z} \langle f | \hat{F}_\alpha | i \rangle \langle i | \hat{F}_\beta | f \rangle \times \text{Im}[\nabla \times \nabla' \times \mathbf{G}(\mathbf{r}_A, \mathbf{r}_A, \omega_L)]_{\alpha\beta} \quad (2.53)$$

In this equation we have also substituted in a representation for the magnetic moment operators acting on the hyperfine manifold using

$$\langle f | \hat{\mu}_\alpha | i \rangle = \mu_B g_F \langle f | \hat{F}_\alpha | i \rangle \quad (2.54)$$

These operators follow the usual angular momentum commutation rules (For07; Hen99).

2.2.8 Spin-flip rate near a normal conductor

The above formalism has been used to calculate the magnetic field fluctuations near various material geometries by solving the Green tensor for the specific boundary conditions.

The free-space lifetime due to blackbody radiation in the far field is given by,

$$\tau_0 = \frac{1}{\Gamma_0^B} = \frac{3\pi\hbar c^3}{\mu_0\omega^3 \sum_{\alpha=x,y,z} \mu_B^2 g_F^2 |\langle f | \hat{F}_\alpha | i \rangle|^2} \quad (2.55)$$

$$= \frac{6\pi\hbar c^3}{\mu_0\omega^3 \mu_B^2} \quad (2.56)$$

which exceeds the age of the universe at room temperature. However, when the atom-surface distance, d , is exceeded by the wavelength of the transition ($\lambda = 2\pi c/\omega \gg d$), the atom is said to be in the near-field of the surface, and the lifetime is reduced considerably from the free space value.

In a geometry typical of an atom chip, with a thin metallic surface layer of thickness h acting as the nearby current carrier, the lifetime is given by Eq. (4) in Ref. (Sch05),

$$\tau_{sf} = \left(\frac{8}{3}\right)^2 \frac{\tau_0}{\bar{n}_{th} + 1} \left(\frac{\omega_L}{c}\right)^3 \frac{d^4}{3\delta_L} \quad (2.57)$$

This expression is valid when $\delta_L \ll d, h$, i.e. the skin depth at the Larmor frequency is much less than either the atom-surface distance or the thickness of the metal layer. The result is equally valid for bulk niobium (the limit of large h), as for the atom chip geometry. It is only when the atom-surface distance drops below the skin depth that distinct scaling behavior is expected. Since the atom-surface distance is $> 20 \mu\text{m}$ in our experiment, while the skin depth is on the order of a few microns, it is reasonable to expect that the above formula is applicable.

Eq. 2.57 has been plotted for several different offset fields at a constant temperature of 4.2 K, and at several different temperatures with a constant offset field of 2.44 G (Fig. 2.3). Whereas increasing the offset field leads to longer lifetimes according to the scaling $\tau_{sf} \propto \omega_L^{3/2}$, increasing the temperature leads to a strong reduction of the lifetime. The scaling is determined by the temperature dependence of the conductivity, which enters into the expression for the skin depth (Eq. 2.25), and by the average thermal occupation which is well approximated by $\bar{n}_{th} \approx k_B T / \hbar \omega_L$ over the entire temperature range considered here. For reference, the skin depth vs. temperature is plotted in Fig. 2.4. The skin depth for OFHC copper (red curve) (E.D) drops from about $50 \mu\text{m}$ at room temperature to less than $5 \mu\text{m}$ at 4.2 K. The corresponding change in the expected lifetime is dramatic, increasing by a factor of 100.

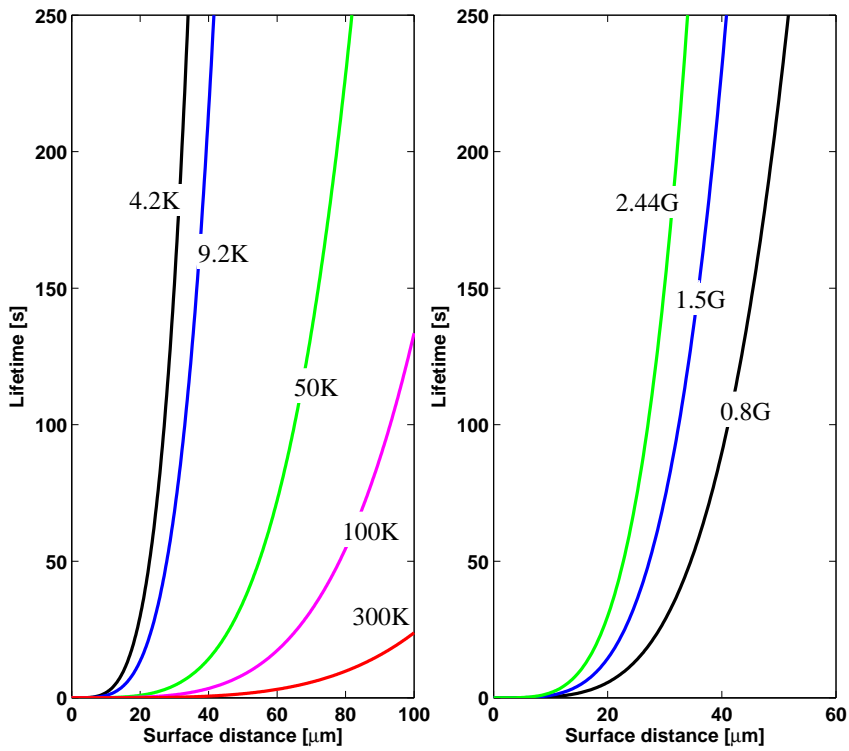


Figure 2.3: *Left:* Theoretical trap lifetime vs. surface distance above a normally conducting slab at several temperatures (with offset field $B_0 = 2.44$ G). *Right:* Trap lifetime vs. surface distance at several offset fields ($T = 4.2$ K)

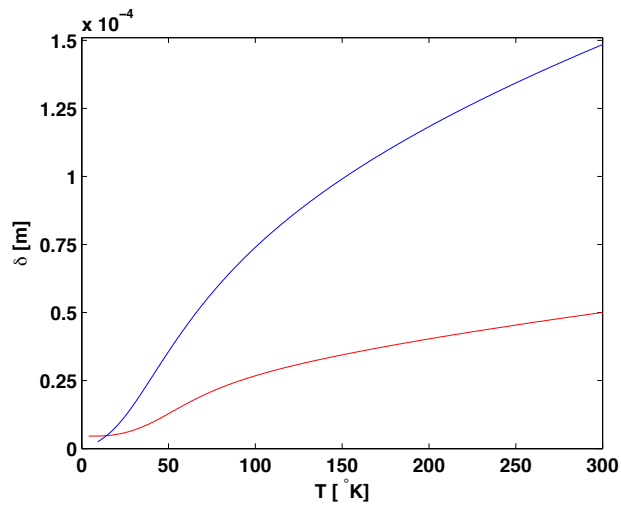


Figure 2.4: The skin depth vs. temperature for copper (red) and normal state niobium (blue). See Fig. 3.7 for a plot of the conductivity data from which this is based.

2.2.9 Spin-flip rate near a super conductor

To derive the scaling behavior of the decay rate of a trapped cloud near a superconductor, Skagerstam et al. consider the dielectric response function of a London superconductor² (Ska06) using a two fluid model. They obtain,

$$\epsilon(\omega) = 1 - \frac{1}{k^2 \lambda_L^2(T)} + i \frac{2}{k^2 \sigma^2(T)} \quad (2.58)$$

This leads to an expression for the transition rate between Zeeman sublevels given by,

$$\begin{aligned} \Gamma_{SC}^B &\approx \Gamma_0^B (\bar{n}_{th} + 1) \left[1 + 2 \left(\frac{3}{4} \right)^3 \frac{c^3}{\omega^3 \sigma^2(T)} \frac{\lambda_L^3(T)}{z^4} \right] \quad (2.59) \\ &= \Gamma_0^B (\bar{n}_{th} + 1) \left[1 + 2 \left(\frac{3}{4} \right)^3 \frac{c^3 \mu_0}{2\omega^2} \left(\frac{T}{T_c} \right)^4 \left(1 - \left[\frac{T}{T_c} \right]^4 \right)^{-3/2} \frac{\sigma \lambda_L^3(0)}{z^4} \right] \quad (2.60) \end{aligned}$$

where the second line is a straightforward algebraic reduction to highlight the expected temperature dependence. The value of $\lambda_L(0)$ enters as a free parameter. Estimating the $T = 0$ London depth to be $\lambda_L(0) = 50$ nm, and with a niobium conductivity $\sigma = 2 \times 10^9 \Omega^{-1} \text{m}^{-1}$ (Cas05), we can estimate the lifetime as a function of temperature. The result is shown for three atom-surface distances of 5, 20, and 50 μm in Fig. 2.5.

Apparently the onset of superconductivity is accompanied by a reduction of the atomic spin flip rate by orders of magnitude. This has been attributed to a combination of effects: electromagnetic screening, a reduced mode volume in which to host fluctuating currents, and the formation of a superconducting gap. In the two fluid model, the reduction of the lifetime from the free space value can be attributed to the finite fraction of thermal electrons. Although the condition for London superconductivity is not necessarily satisfied at low temperatures, so far only local media have been considered. As was mentioned, non-local effects can be accounted for phenomenologically by considering an increase in the $T = 0$ London penetration depth.

The two fluid model does not account for the quasi-particle states arising from thermal fluctuations. Hohenester et al. (Hoh07) provide an analysis, deriving an expression for the optical conductivity in the framework of BCS theory, which allows for quasi-particles, and Eliashberg theory, which additionally accounts for the absorption and emission of real phonons.

²A London superconductor is one for which $\lambda_L \gg \xi_0$. For a slab of pure niobium, measurements give $\xi_0 \approx 38$ nm

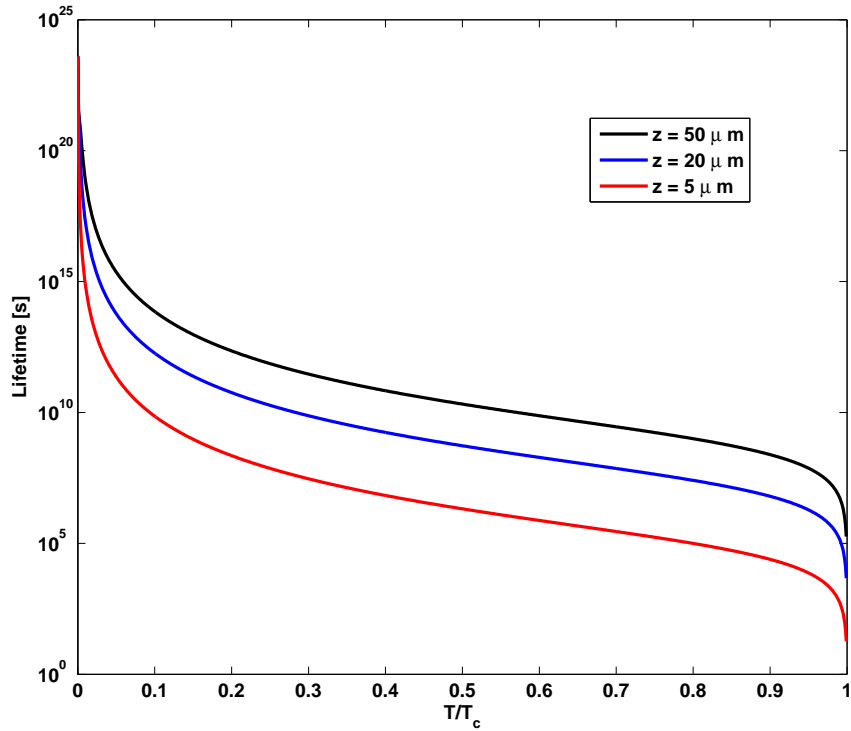


Figure 2.5: The lifetime near a superconducting slab in dependence of temperature. The inability of a superconducting electrons to host electromagnetic fluctuations below the energy gap (2.1 THz for niobium with $T_c = 9.2\text{K}$), combined with electromagnetic screening leads to orders of magnitude enhancement of the lifetime below T_c .

Chapter 3

Experimental apparatus

In this chapter, we present an experimental setup which was designed and built in order to realize a superconducting microtrap for ultracold atoms. The key elements of the apparatus are shown in Fig. 3.1.

3.1 Vacuum System

In order to sufficiently insulate a cold atomic cloud from the room temperature environment, the vacuum system must be able to continuously pump to pressures around 10^{-11} mbar. Reaching UHV pressures (anything below 10^{-9} mbar) requires various types of pump, and presents several challenges. Great care must be taken to avoid introducing parts, materials or contaminants that are not UHV compatible (nas). Each part must be cleaned before entering the UHV. The standard procedure involves an hour or more in an ultrasonic bath, first with Tickopur RW 77 (a specialty cleaner for ultrasonic baths), then with Acetone, and lastly with methanol or isopropyl alcohol. Finally the entire chamber has to be baked out at 140°C or more (taking care not to exceed the maximum bakeout temperature of sensitive components). The bakeout typically lasts for at least one week, or until the pressure stabilizes.

3.1.1 Vacuum Chamber

We designed the vacuum chamber in order to combine an experimental setup suitable for preparing clouds of ultracold atoms, with a cryogenic environment in which low temperature superconductivity could be achieved. The design work was done using the Solidworks CAD program, and the chamber itself was machined by Hositrad with two in-line valves welded into place (to reduce the tube length). A schematic of the chamber and pumps is shown in Fig. 3.2. It shows the main chamber, the various pumps (Rough pump, TMP, TSP, IP), and the locations of pressure sensors (VM). The cryostat enters at a flange 670 mm above the cold finger surface. The vertical position of the cold finger can be coarsely adjusted by a Z-translator (Z-trans.). The preparation of ultracold atoms occurs

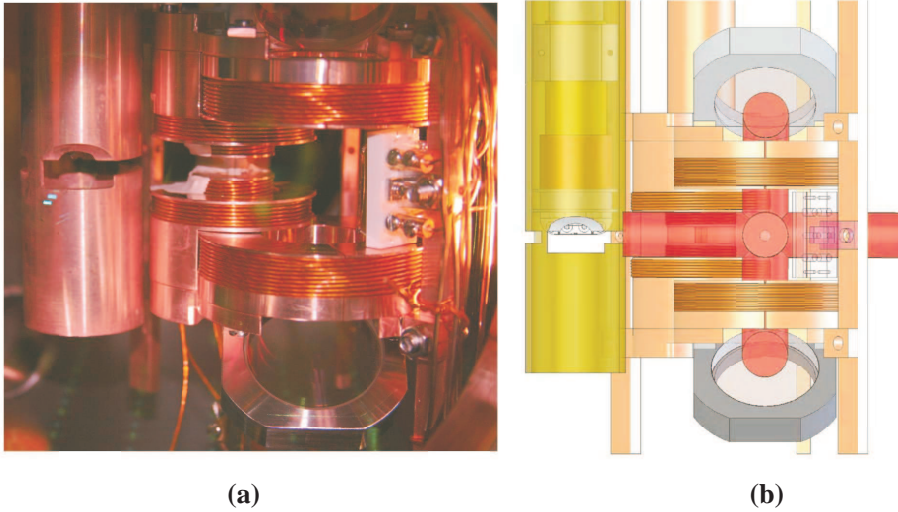


Figure 3.1: (a): Inside setup photo showing the cryostat shielding (left) and the adjacent BEC apparatus (right) as seen from the front viewport. (b): A CAD graphic showing the same structures. The cryostat shielding has been made partly transparent for display purposes. The 6 MOT beams, shown in red, enter the chamber from 4 directions. A pair of dispensers mounted nearby enhances the loading rate.

adjacent to the cryostat, in a thermally separate setup. The electrical feedthroughs (EF) on the top flange supply the in-vacuum conductors used to capture and cool a cloud to temperatures of a few μK . The large front view port provides broad optical access.

The chamber is made of stainless steel, and all seals (out to the TMP exhaust) are between a pair of ConFlat (CF) flanges, and a ring of oxygen-free high conductivity (OFHC) copper which is placed concentrically between them. As the flanges are screwed together, the knife edge of the flange is forcibly pressed into the softer OFHC copper. This type of seal is a similar to the principle behind in-line valves, where the knife edge can be repeatedly separated and re-engaged with a copper ring (the Thermionics valves in use accept a torque range from 12 to 25 ft · lbs). These metal-metal seals are very effective, and enable UHV pressures, however leaks can arise from defects. We inspected knife edges and copper rings, and cleaned them with acetone, isopropyl alcohol, and compressed air immediately before use.

3.1.2 Vacuum Pumps

The approximate operating range and achievable pressures of the various vacuum pumps employed in our chamber setup are listed in Table 3.1. Note that these values are specific to the types of pump, and exact configuration of our experiment, and should not be considered general. For a detailed account, see Ref. (O'H03).

From the central science chamber, a bakeable straight through (in-line) UHV valve leads to a pumping stage, consisting of a turbo-molecular pump (TMP) and a diffusion

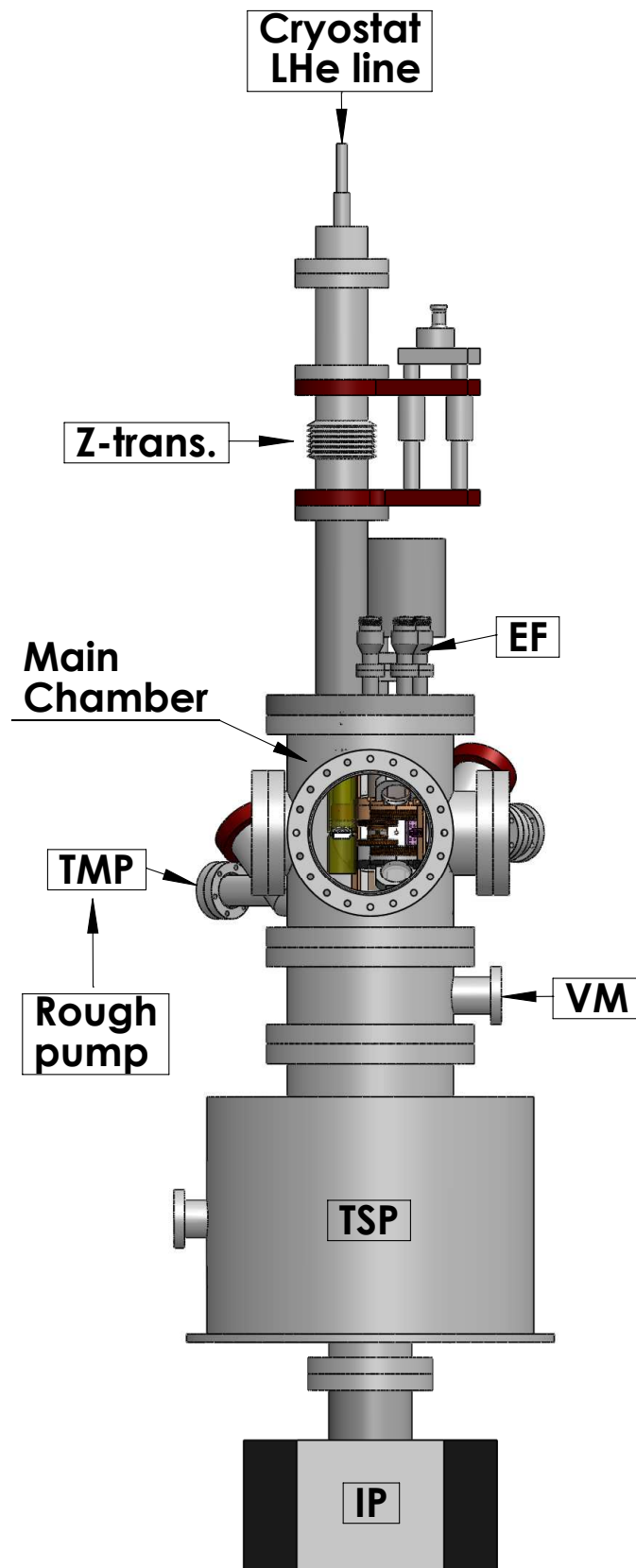


Figure 3.2: Schematic of the vacuum system showing the main chamber, cryostat, pumps and sensors.

Table 3.1: Pump pressure guide for the vacuum chamber (units: mbar).

Pump type	Operating range	Min. pressure (pre-bake)	Min. pressure (post-bake)
Rough	$10^3 - 10^{-4}$	1×10^{-3}	NA
Turbo-Molecular (TMP)	$10^{-2} - 10^{-10}$	1×10^{-6}	5×10^{-9}
Ion (IP)	$10^{-5} - 10^{-12}$	1×10^{-7}	1×10^{-12}
Ti-sublimation (TSP)	$10^{-8} - 10^{-12}$	NA	1×10^{-12}

(rough) pump connected in series. The exhaust of the TMP forms the intake of the rough pump with a Klein Flange (KF) valve between them. The rough pump is not an oil free pump, meaning that (bakeable) filters are also needed in this section to insure no oil vapors enter the chamber. Exhaust from the rough pump is led to an exhaust outlet and removed from the lab.

Using this setup, we can pump to high vacuum pressures. To reach UHV, additional pumps are required. In parallel with the TMP and rough pump, an ion pump (IP) and titanium sublimation pump (TSP) are connected below the chamber. We use a Varian VacIon plus Starcell 75 IP which uses large electric fields to ionize and accelerate gas molecules into a getter material such as titanium. A strong magnetic field causes the charged particles to move along helical paths, increasing the ionization efficiency (O'H03). The TSP is a type of getter pump where background gas molecules are absorbed by the pump's reactive metal walls. The gas either diffuses into the metallic layer, or reacts to form non-evaporable compounds. The IP and TSP have no moving parts and are therefore able to be run continuously during experiments without causing mechanical vibrations.

3.1.3 The road to UHV

After sealing the chamber, the rough pump was switched on. The TMP can operate at 1bar, but only becomes efficient at pressures below 10^{-3} mbar or so. With both pumps operating, pre-bakeout pressures of below 10^{-6} mbar were possible.

The next step was to bake the chamber. Numerous heating tapes were wound around the chamber, with several strategically placed temperature sensors. The entire chamber was then wrapped in aluminum foil. We used controllers to monitor and regulate the temperature. We then slowly increased the temperature ($5 - 10$ °C/hour) to between 150 and 200 °C. The IP can be switched on during this phase as long as the pressure does not exceed a few 10^{-5} mbar. Arcing may occur if the pressure is too high. In general ion pumps should be switched on at the lowest possible pressure to extend their lifetime. After a week at high temperature, when the pressure had stabilized, the chamber was cooled slowly back to room temperature in about 3 days. The vacuum improved dramatically during this phase reaching a few 10^{-10} mbar.

The final stage for producing UHV utilized the TSP. The principle of its operation is as follows: a current of 50 A for up to 30 seconds is applied to a titanium wire which extends into the central region of the chamber. Resistive heating causes the titanium to become very hot. Sublimation occurs and the titanium particles stick to the chamber walls. After an initial climb, the pressure typically falls rapidly due to efficient getter pumping. Regular titanium flashes (at least once per month) were applied to re-coat the chamber walls, usually after filling the pump with liquid nitrogen. Operating the pump with liquid nitrogen had little effect on the pressure during experiments at cryogenic temperatures. This is because the cryostat itself acts as an even more efficient vacuum pump in the region of the atoms. The pumping mechanisms, cryocondensation and cryosorption, can effectively pump a wide range of gases, including hydrogen (O'H03). Furthermore, outgassing from cryogenic surfaces is completely negligible. These are significant advantages conferred by including in-vacuum cryogenics.

3.1.4 Background pressure

In practice, it is impossible to create a perfect vacuum due to leaks, outgassing, hydrogen and helium diffusion through the metal walls, and pump limitations. In addition, during experiments, rubidium is heated from a dispenser releasing thermal rubidium atoms as well as molecular "dirt" which briefly contaminate the chamber. Continuous measurement of the vacuum can be taken below 10^{-4} mbar by a pressure sensor between the main chamber and the TSP. It was often the case that pressures below 10^{-11} mbar were measured while operating the cryostat. After opening and resealing the chamber in June 2008, the best obtainable pressure rose slightly to about 3×10^{-11} mbar.

During the measurements presented in Sect. 4.2, the vacuum limited lifetime of the atomic cloud allows us to estimate the background vacuum in the region of experiments. The residual background gas density n_{bg} leads the atom number to decay on a time scale, $1/\tau_{bg} = n_{bg}\sigma_{bg}\bar{v}_{bg}$, where the average particle velocity is \bar{v}_{bg} 1000 m/s at room temperature, and σ_{bg} 10^{-13} cm² is the background cross section (Wei03a). The observed decay rate of $\sigma_{bg} = 0.006$ s⁻¹ puts an upper limit on the background vacuum pressure of about 6×10^{-11} mbar.

3.2 BEC apparatus

In this section, we describe UHV compatible apparatus capable of cooling a ⁸⁷Rb cloud to quantum degeneracy. During normal operation, this device was used to cool an atomic cloud of 2.5×10^6 atoms to a temperature 1 μ K. For a description of the procedure used, see Sect. 3.7.

3.2.1 In-vacuum setup

We have constructed an in-vacuum BEC apparatus, which is used to prepare an ultracold cloud for transport to the cryogenic region. The construction is attached to the top flange, and is powered via three electrical feedthroughs there. This entire setup is at room temperature, with a 19 mm diameter OFHC copper rod acting as a heat sink. In this way, the heat generated by the coils (which can exceed 30 W during evaporative cooling) is removed from the chamber. A two-component UHV compatible ceramic glue was used to improve the thermal contact between, e.g. the coil holders and the wires.

All coils are wound with 1 mm thick kapton-coated wire. The coil holders were made in-house by machining OFHC copper. Thin radial extruded cuts were made to minimize the formation of eddy currents while switching on and off current. The setup consists of three coil pairs and a pair of vertical adjacent wires. The MOT coils consist of 151 windings each (height 10 mm, inner/outer radius 16.5/32 mm), with a center-to-center separation of 42 mm. The transfer coils consist of 50 windings each (height 6 mm, inner/outer radius 12.5/24 mm), with a center-to-center separation of 24 mm. The Ioffe coils consist of 46 windings each (height 10 mm, inner/outer radius 5.5/12 mm), with a center-to-center separation of 18 mm. The Ioffe wires are actually a single 1.5 mm diameter OFHC copper wire which doubles back. They run parallel and equidistant to the Ioffe (and transfer) coil axes, but are each offset by about 3 mm.

The reason for this elaborate construction is ultimately to avoid Majorana losses during evaporative cooling (Bri06). The magnetic trap formed by the MOT coils alone has a quadrupole minimum (magnetic field zero), and in this region, atoms which violate the adiabatic condition are lost from the trap. An Ioffe trap, with its finite field trap minimum, makes this loss process negligible. However, creating an Ioffe trap requires the inclusion of additional magnetic field generating elements: in this case an Ioffe wire pair. It is difficult to include such elements directly adjacent to a MOT while maintaining optical access. The magnetic transfer alleviates this problem. In addition, the Ioffe coils allow the trap to be compressed increasing the trap frequencies, and hence the cooling efficiency.

After the transfer, the Ioffe trap frequencies were measured to be $\omega_r/2\pi = 272$ Hz radially, and $\omega_a/2\pi = 45$ Hz axially. The offset field at the trap minimum is approximately 1 Gauss. To realize evaporative cooling in the Ioffe trap, we apply a radio frequency sweep (source: BK precision rf generator), from an initial value of 15 MHz down to 1 MHz (at constant amplitude) over 10 to 16 seconds. The circuit used to add the rf signal onto the Ioffe wires is shown in Fig. 3.3. Long evaporation times improve the efficiency of the process and ensure that the cloud remains in thermal equilibrium.

Once cooled to about 1 μ K, the atoms can efficiently be loaded into an optical dipole trap. The procedure requires a careful alignment of the optical trap focus with the Ioffe trap center. A discussion can be found in Sect. 3.4.3.

We performed extensive magnetic field simulations to better understand the magnetic

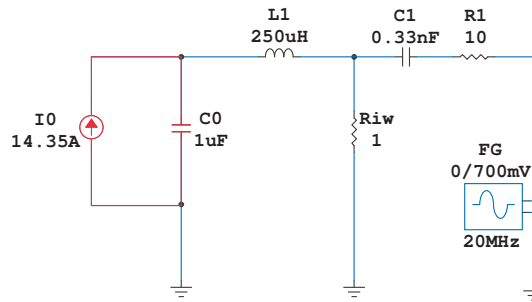


Figure 3.3: Circuit used for adding a radio frequency to the Ioffe wires (with resistance R_{iw} in Ohms). The circuit uses a capacitance ($C1$) to transmit rf onto the wires while protecting the function generator from the High Finesse (15 A) dc current supply (in red). Inductance ($L1$) is a low pass that directs the rf onto the Ioffe wires.

transfer and Ioffe trap formation. For this, I wrote a library of routines in Matlab, with which wires and coils can be modeled. The latter relies on exact formulas for the field of a current loop, calculated using elliptic integrals. This code (for a single current loop) is reproduced in Appendix A.

3.3 MOT overview

Central to nearly all cold atom experiments is the magneto-optical trap (MOT). The first MOT is described by E.L. Raab and colleagues at Bell Laboratories (Raa87). By illuminating a spherical quadrupole magnetic field with counter propagating, circularly polarized beams from orthogonal directions (see Fig. 3.4), they could trap and cool sodium atoms to temperatures as low as $300 \mu\text{K}$. The exact dynamics of a MOT are complex, with many regimes to consider (Tow95). Roughly speaking, cooling occurs due to the Doppler shift, whereby atoms of a certain velocity class are blue-shifted into resonance with the oncoming beam (which is red-detuned from resonance). Trapping arises from the Zeeman effect. Atoms that are displaced from the zero of the quadrupole preferentially absorb that beam which kicks them toward the trap center. For rubidium, the minimum cloud temperature according to the Doppler limit is $\hbar\gamma/2k_B = 145 \mu\text{K}$, where $\gamma = 2\pi \times 6.07 \text{ MHz}$ corresponds to the D2 transition linewidth (Steb).

Early experiments with MOTs demonstrated cloud temperatures lower than the Doppler limit (Let88; She89). This was attributed to polarization gradient cooling, or Sisyphus cooling. The effect has been explained for the case of both $\text{lin} \leftrightarrow \text{lin}$ and $\sigma^+ \leftrightarrow \sigma^-$ (Dal89). In both cases, the counter propagating beams form a standing wave. The mechanism governing the cooling, however, is different. With $\sigma^+ \leftrightarrow \sigma^-$ (relevant to our experiment), the polarization is linear but rotates along the beam axis in a helix. The atomic electric dipole moment aligns with the electric field. With cold atoms, the atomic polarization easily follows the rotating electric field. In the rotating frame of the atoms, this introduces

a term which resembles a constant magnetic field along the beam direction. As an atom travels along the beam path it is optically pumped and preferentially occupies a state with a higher probability of absorbing the oncoming beam (as determined by the different Clebsch-Gordan coefficients). This leads to a drag force with a net cooling effect. In theory, the minimum achievable temperature, $T_{recoil} = 2E_{rc}/k_B$ of 362 nK for ^{87}Rb is limited by the recoil energy, $E_{rc} = \hbar^2 k^2 / 2m$, associated with the wavevector k of the photon emitted by the atom. In practice such temperatures are difficult to attain due to radiation trapping within the MOT (Cas98). Subsequently, narrow-line cooling of strontium was used to reach the recoil temperature in a MOT (Kat99).

3.4 Laser system

In this section we describe the MOT laser system, and the imaging setup in our experiment. The spectrum of rubidium can be found in Figure B.1 of the Appendix.

3.4.1 Laser components

Two types of lasers were constructed: grating stabilized (master) lasers, and injection locked (slave) lasers. The master lasers use a grating injection scheme known as the Littrow configuration, detailed in Ref. (Ric95). In this setup, the first order of the diffracted beam is coupled back into the diode forming a resonator. To perform an injection lock, a portion of the light from a master laser is spatially overlapped with the outgoing beam of the slave laser operating in the same frequency range. This results in a mode matching whereby the slave laser follows the master laser, essentially amplifying the master laser output.

Different diodes were used for these two locking methods. Hitachi (part no: HL7851G) have moderate output power (about 50 mW) but provide a linewidth of less than 1 MHz. These lasers are appropriate for rubidium spectroscopy, and as master lasers for injecting other diode types. For the slave lasers we used diodes from Sharp (part no: GH0781JA2C). These diodes provide higher output power (about 100 mW) but are not ideal for spectroscopy due to a broader linewidth. A tapered amplifier (TA) acts much like a slave laser, but is capable of higher output power. We injected a TA from Eagleyard Photonics, which produces an output power of 500 mW.

These output powers do not take into account the losses at the various components. Optical isolators (optical analogs of diodes) have transmission coefficients of 90% or less. Standard components like mirrors, lenses, and λ -plates, though anti-reflection coated, scatter a small fraction of the incident beam. Finally, single-mode optical fibers are a major source of loss, rarely transmitting more than about 50%. Polarization maintaining fibers have been used throughout, lessening the sensitivity of the fiber itself to mechanical vibrations. But the in-coupling remains sensitive to small mechanical drifts, which typically arise from temperature changes in the lab.

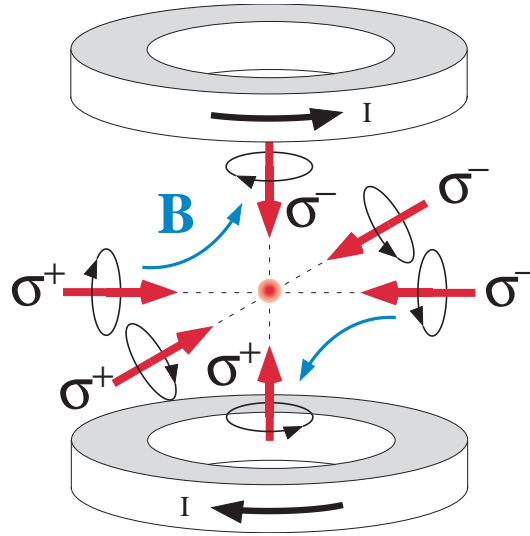


Figure 3.4: MOT diagram showing the orientation of magnetic fields and light polarizations. The magnetic field (blue) is cylindrically symmetric about the coil axes. The top and bottom beams consist of σ^- and σ^+ light respectively, however, these do not correspond to opposite polarization in the lab frame (rather to the reversal of the quantization axis that occurs at the MOT center). It should be noted that the polarization of the vertical beams (e.g. right circular) is opposite to that of the horizontal beams (left circular) in the lab frame.

3.4.2 MOT light

The MOT light entering the chamber in 6 beams consists of 100 mW cooling overlapped with 20 mW repumping light. The top and bottom MOT beams enter through the large (CF150) front viewport. They are reflected by a pair of in-vacuum dielectric mirrors mounted with aluminum holders on the coil setup (the details of which are presented in Sect. 3.2). The cooling light, 18 MHz red-detuned from the $|5S_{1/2}, F = 2\rangle \rightarrow |5P_{3/2}, F = 3\rangle$ transition, has a wavelength 780.24606 nm. The repumper addresses those atoms which land in the state $|5S_{1/2}, F = 1\rangle$. From the selection rules it is clear that these are atoms that experience off resonant excitation $|5S_{1/2}, F = 2\rangle \rightarrow |5P_{3/2}, F = 2\rangle$ from the cooling beam, only to subsequently decay to $|5S_{1/2}, F = 1\rangle$. The repumper illuminates the $|5S_{1/2}, F = 1\rangle \rightarrow |5P_{3/2}, F = 2\rangle$ resonance, with wavelength 780.23268 nm. Both cooling and repumping beam consists of circularly polarized light with the same orientation, depicted in a diagram of the MOT in Fig. 3.4.

The exact method for producing the correct frequencies is somewhat arbitrary. We have built standard polarization spectroscopies using the feedback of the difference signal of a photodiode pair to adjust the Laser's diffraction grating angle. The repump laser is locked to the repumper frequency, while the reference laser is locked to the $|5S_{1/2}, F = 2\rangle \rightarrow |5P_{3/2}, F = 2/F = 3\rangle$ crossover peak in the hyperfine structure of ^{87}Rb at 780.24629 nm. This light is split and frequency shifted with acousto-optic modulators (AOMs). By shift-

ing the frequency +133 MHz, the light is resonant with $|5S_{1/2}, F = 2\rangle \rightarrow |5P_{3/2}, F = 3\rangle$, and is used for imaging (with linear polarization). By shifting -133 MHz we reach the $|5S_{1/2}, F = 2\rangle \rightarrow |5P_{3/2}, F = 2\rangle$ transition. This optical pumping light enters the chamber after it is overlapped at a beam splitter with the lower MOT beam and likewise imbued (σ^+) circular polarization by a $\lambda/4$ -plate. The optical pumping beam has $500 \mu\text{W}$ power and lasts for $80 \mu\text{s}$. The OP AOM not only shifts the frequency, but can act as a fast shutter with switching times less than $1 \mu\text{s}$. It is used in combination with a physical shutter to guarantee full beam extinction.

The optical pumping light is nearly 267 MHz red-detuned from the imaging frequency. It acts as a reference for the generation of a beat signal with the MOT master cooling laser. We lock the beat signal at 248 MHz, thus giving the above stated detuning of just over 18 MHz during the MOT capture phase. By biasing the lock point, we can vary the MOT detuning by more than 75 MHz. This has allowed us to implement polarization-gradient (Sisyphus) cooling.

Light from the MOT master laser is used to inject a tapered amplifier (TA) with up to 40 mW. The tapered amplifier output is specified as 1 W, however following an optical and a single mode fiber, it produces nearly 200 mW, which is more than enough to power the MOT. A schematic layout of the laser system for the MOT and imaging can be seen in Fig. 3.5.

3.4.3 Optical dipole trap and transfer

The optical tweezers, also referred to as optical dipole trap (ODT), is a versatile tool for trapping particles ranging in size from the atomic scale (sub-nm) to several microns. No magnetic fields are required, making it a technique ideally suited to studying, e.g. Feshbach resonances in atomic systems (Cou98), in which homogeneous magnetic fields can be used to tune the scattering length. We also find it the optimal tool for quickly transporting thermal clouds to the cryogenic trap without introducing an additional heat load.

The trapping of an atom by a focused, red-detuned laser can be understood by considering the interaction of the atomic ground state with the laser field. In the dressed state scenario, a two level atom with transition frequency ω_0 , and a driving laser with frequency ω leads to a light shift of the ground state given by I/Δ , where $\Delta \equiv \omega - \omega_0$. For a laser red-detuned from resonance ($\Delta < 0$), the shift is negative, and it is energetically favorable for atoms to reside in the region of highest intensity. A focused laser beam, with its gaussian intensity profile $I(r)$ leads to a harmonic potential to second order both axially and radially.

Following Grimm et al. (Gri99), we use the classical damping rate, Γ , to determine the potential and scattering rates,

$$U_{dip}(r) = -\frac{3\pi c^2}{2\omega_0^3} \left(\frac{\Gamma}{-\Delta} + \frac{\Gamma}{\omega_0 + \omega} \right) I(r) \quad (3.1)$$

3.4. Laser system

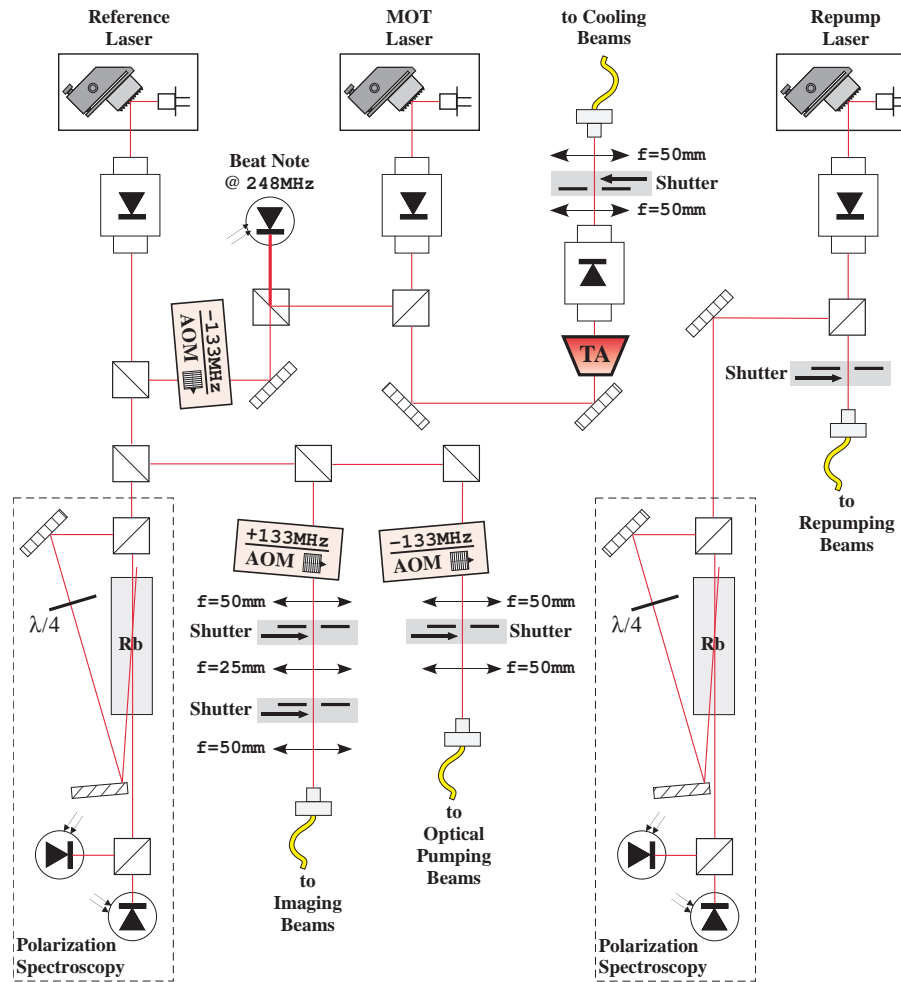


Figure 3.5: Optical table setup schematic showing the lasers used for creating a MOT (consisting of cooling and repump beams overlapped after the fibers). Also shown are the various components used to generate light for optical pumping and imaging.

$$\Gamma_{sc} = -\frac{3\pi c^2}{2\hbar\omega_0^3} \left(\frac{\omega}{\omega_0}\right)^3 \left(\frac{\Gamma}{-\Delta} + \frac{\Gamma}{\omega_0 + \omega}\right)^2 I(r) \quad (3.2)$$

For simulating the ODT we use the full semi-classical equations. The rotating wave approximation has *not* been employed since it underestimates the trap depth by about 10%.

We used a IPG ytterbium fiber laser with $\lambda = 1064$ nm, operating with 0.7 W of output power. A single beam was focused through an AOM which was primarily used as a shutter: the intensity of the deflected beam is proportional to the applied rf-power. We also demonstrated that by modulating the applied rf-frequency, the atomic cloud could be shifted by up to 100 μ m (limited by the size of the optics). However, this heated the cloud and was therefore not employed during experiments.

Alignment of the ODT with the Ioffe trap was accomplished as follows. First the ODT beam was approximately positioned to the position of the Ioffe trap by observing with an IR viewer that it struck the Ioffe wires at the place. A weak $|5S_{1/2}, F = 2\rangle \rightarrow |5P_{3/2}, F = 3\rangle$ resonant beam was carefully overlapped with the ODT beam. Then the experiment was run in order to prepare an ultracold cloud in the Ioffe trap. The resonant beam was used to illuminate the atoms for about 0.25 s, causing them to be heated rapidly and ejected from the trap. The better the spatial overlap with the cloud, the fewer atoms were observed in subsequent absorption images. As the overlap is improved by adjustments to the ODT lens (mounted on a three-axis translation stage), the power was reduced accordingly to sharpen the atom number minimum. Ultimately, about 1 μ W was sufficient. Once this alignment was performed, the experiment was run using the fiber laser in place of the resonant beam. At this stage, usually the effect of the ODT beam could be observed, and must then be aligned to optimize the Ioffe to ODT loading. Loading into the ODT typically heated the cloud from 1 μ K to about 1.5 μ K. This is likely a result of the mode mismatch of the Ioffe and optical dipole traps.

The final mirror and lens with focal length $f = 250$ mm are mounted on a translation stage with 50 mm travel. An air bearing stage (Aerotech ABL 1000) is used to minimize mechanical vibrations. Such vibrations are known to be responsible for heating atomic clouds in optical traps (Sav97; Geh98).

After loading the cloud into the optical tweezers, the acceleration of the stage was ramped sinusoidally. The total travel of 44 mm takes place in 570 ms. Once positioned near the cryostat the cloud was loaded into the niobium wire trap by ramping up the magnetic potential, and subsequently ramping down the optical tweezers power.

3.5 Cryogenic trap

Here we describe the cryostat, and our setup which enables loading from an optical dipole trap into a superconducting microtrap operating at temperatures of 3 to 8.5 K.

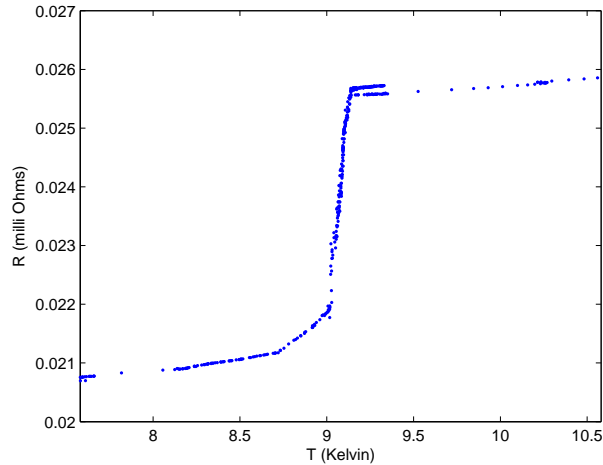


Figure 3.6: This graphic shows the measured transition in the niobium wire from normal to superconductor. This measurement was made using a GPIB compatible current supply, and voltage readout in the 4-point configuration. The resistance drop occurs at the onset of superconductivity below 9.14 K. At 9.02 K, the wire is fully superconducting, and current no longer flows through the copper shunt.

3.5.1 Cryostat

The cryostat (Janis ST-400) delivers a continuous flow of liquid helium to a copper cold finger inside the vacuum chamber. To power experiments near the cryogenic surfaces, two electrical feedthroughs enter the cryostat flange. The liquid helium source is a helium can which holds 100 L, enough for 4 days of experiments at 4.2 K. Liquid helium flows to the cold finger through a transfer line. This transfer line consists of a flexible metal tube evacuated to 10^{-6} mbar. Inside, another flexible metal tube surrounded by spacers and radiation shielding carries the liquid helium. The line leads into the cryostat through an elongated nozzle. The helium boils atop the cryostat cold finger, then travels out through an exhaust line where it is recycled. In this way the cold finger can be cooled below the transition temperature of niobium, measured to be 9.02 K (see Fig. 3.6).

The nominal cooling power of the cryostat at 4.2 K is 3 W, sufficient to keep the cold finger in thermal equilibrium during experiments. We note that lower cryostat temperatures (down to 2.8 K) can be achieved by evacuating the helium exhaust. However this increases the helium consumption dramatically from 1 ℓ /hour to nearly 2 ℓ /hour. Alternatively, above the boiling point of helium, a resistive heater at the cold finger allows us to stabilize the temperature with a temperature controller to within 0.5 °K.

The cold finger is surrounded by a gold plated copper radiation shielding. A small cut-out in the shielding allows optical access for the optical tweezers and imaging. The shielding is cooled by the helium exhaust to ≈ 25 K. This shielding works by reflecting and absorbing the blackbody radiation from the surroundings. To quantify the power we

use the Stefan-Boltzmann law, which states that the power per unit area is $P/A = \sigma \times T^4$, where the factor $\sigma = 5.6704 \times 10^{-8} [\text{W}/\text{m}^2 \text{K}^4]$ is Stefan's constant, and T is the body's temperature. The shielding prevents $0.05 \text{ W}/\text{cm}^2$ or about 5 W total of radiation power from impinging the cryostat.

Thermal conduction, and electrical resistance are other potential heat sources. In UHV, and at cryogenic temperatures, thermal heat sinking becomes a significant challenge. This is due to a lack of tested materials that can provide high thermal conductivity interfacing. As a solution, each wire leading from the electrical feedthroughs was pressed between two copper heat sinks attached to the cryostat at four locations along the 670 mm length. The final heat sink is attached just above the shielding and is assumed to be at $T = 30^\circ \text{K}$. Each wire that leads to the wire trap is wound so as to decrease the thermal gradient. To minimize thermal conduction, long thin wires are ideal, while resistive heating is minimized by short thick wires. We use 1 mm diameter kapton coated wires for the majority of the length of the cryostat. After the final heat sink, thinner wires ($120 \mu\text{m}$) are used to supply the wire trap.

It is possible to calculate the thermal conductivity characterized by electrical conductivity data using the Wiedemann-Franz Law: the ratio of thermal (κ) to electrical (σ) conductivity of a metal is directly proportional to the temperature,

$$LT = \kappa/\sigma \tag{3.3}$$

The constant $L = 2.45 \times 10^{-8} [\text{W}\Omega/\text{K}^2]$ is called the Lorenz number. The electrical conductivity of OFHC copper is known from (E.D). There is also data for normal conducting niobium, where superconductivity is quenched below $T = 9.25^\circ \text{K}$ by a large external magnetic field (Web69). In each case, a fifth order polynomial fit functions to the measured electrical conductivity has been extrapolated. The electrical and associated thermal conductivities are shown as a function of temperature for niobium (blue) and copper (red) in Fig. 3.7. It is interesting to note that the electrical (and thermal) conductivity of niobium exceeds that of copper at $\approx 15^\circ \text{K}$, well before the superconducting transition.

With the onset of superconductivity, the thermal conductivity is no longer dominated by the electronic contribution, but rather by lattice phonons (Buc04), resulting in negligible heat transport.

Let us assume that the wires can thermalize to the heat sinks on the cryostat. To approximate the heat flow along the wires, we estimate the temperature difference ΔT between two points separated by a length of wire Δx . For a wire with cross sectional area A , the amount of heat ΔQ which flows per unit time Δt is $\Delta Q/\Delta t = A\kappa\Delta T/\Delta x$ where κ depends on the temperature and therefore the position. This leads to a differential equation that can be solved using finite-difference methods. Commercial software such as Comsol is well suited to this task. We are only concerned with the heat that reaches the cold finger. Between $T = 30^\circ \text{K}$ and $T = 4^\circ \text{K}$, the heat flow along 20 centimeters of $120 \mu\text{m}$ diameter copper wire is just 3 mW . This can be compared with the resistive

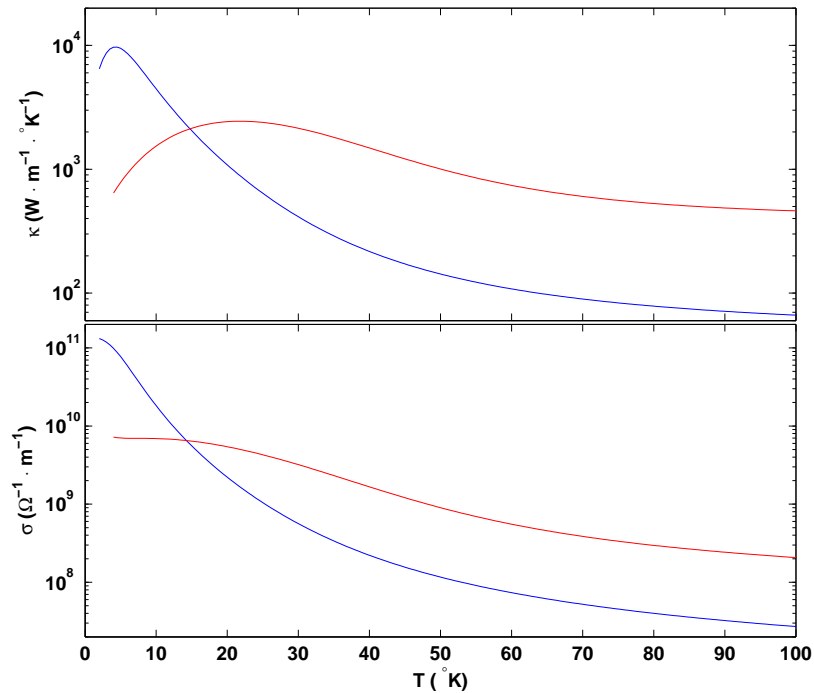


Figure 3.7: *Top:* Thermal conductivities are calculated using the Wiedemann-Franz Law in eq. 3.3. *Bottom:* Best fit to data for the electrical conductivity of copper and niobium.

heating of 5mW/A/cm which for typical operating currents plays a more dominant role.

The thermal connection between the cryostat and the wires is crucial. Early trials with Stycast and silver paste were unsuccessful in reaching the superconducting transition. To ensure a good thermal contact between the niobium wire and cold finger, the entire length of the straight niobium wire is clamped by solid copper (with the exception of a 1 mm gap along the wire axis to allow clearer imaging access near the niobium surface. See Sect. 3.5.2 for further details).

3.5.2 Cryogenic wire trap

We now describe the cryogenic wire trap. The setup allows comparative measurements of the lifetime near a superconductor or normal metal to be performed in close proximity. However, there is a significant drawback with this setup, namely that we are unable to form a trap when the niobium wire is above its transition temperature.

At the copper cold finger, we attached a copper mount, pictured in Fig. 3.8. This mount has adjacent copper plates which can be pressed together by screws. In this way, the entire length of the straight niobium wire is clamped by solid copper (Fig. 4.6), except for a 1 mm gap along the wire axis where the whole wire is free-standing. This provides free optical access for imaging the atoms just below the wire surface.

Atoms are loaded into a Ioffe type microtrap, which is created by a superconducting

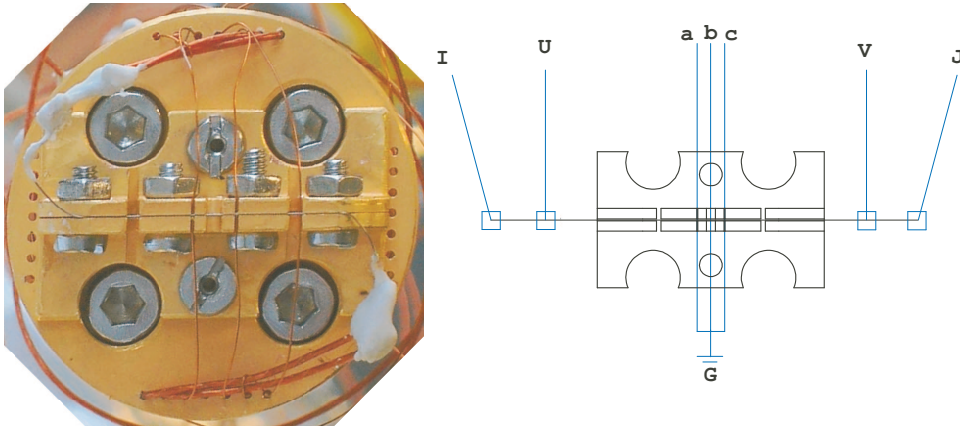


Figure 3.8: Photo (*left*) of the copper mount attached to the cold finger of the cryostat during measurements of the Meissner effect (Sect. 4.1). After opening the chamber, the right-most of the three vertically oriented capping wires was moved to the middle region. A schematic of the connection scheme (*right*) shows the wire trap configuration during lifetime measurements. The niobium wire current flows from I to J. A four-point measurement was possible by measuring the voltage across U-V. The capping wires labeled a,b, and c provided axial confinement.

niobium wire of radius $R = 62.5 \mu\text{m}$, plus externally applied bias (B_x) and offset (B_y) fields generated by coils external to the chamber. Additional wires running parallel to the x -axis are used to increase the axial confinement and evaporative cooling efficiency. The procedure for trap loading is discussed in Sect. 3.7, and a time series plot is shown in A.2

This microtrap is used to bring atoms close to the cold surface, where we measure the spin coherence time of atoms near superconducting niobium and normal conducting copper separately, but in close proximity.

3.6 Imaging

Absorption imaging is the leading method for gaining information about cold atomic cloud properties. For this reason, the topic has been covered extensively by numerous authors. It should be noted that a stable frequency is crucial for this type of resonant imaging, since fluctuating frequency maps to fluctuations in the observed atom number. Likewise it is very important to keep the intensity constant to prevent unwanted offsets. Where applicable, we have removed these offsets during the gaussian fitting routine.

Fig. 3.9 shows a view inside the chamber from above encompassing the region of the Ioffe, optical dipole, and superconducting traps. Imaging in the SCMT typically takes place along axis #2 (x -axis) during experiments. However, using a set of replaceable optics, axis #1 (y -axis) could image both the Ioffe trap, and the SCMT. The latter was used for the angular calibration which allowed us to determine the cloud surface distance

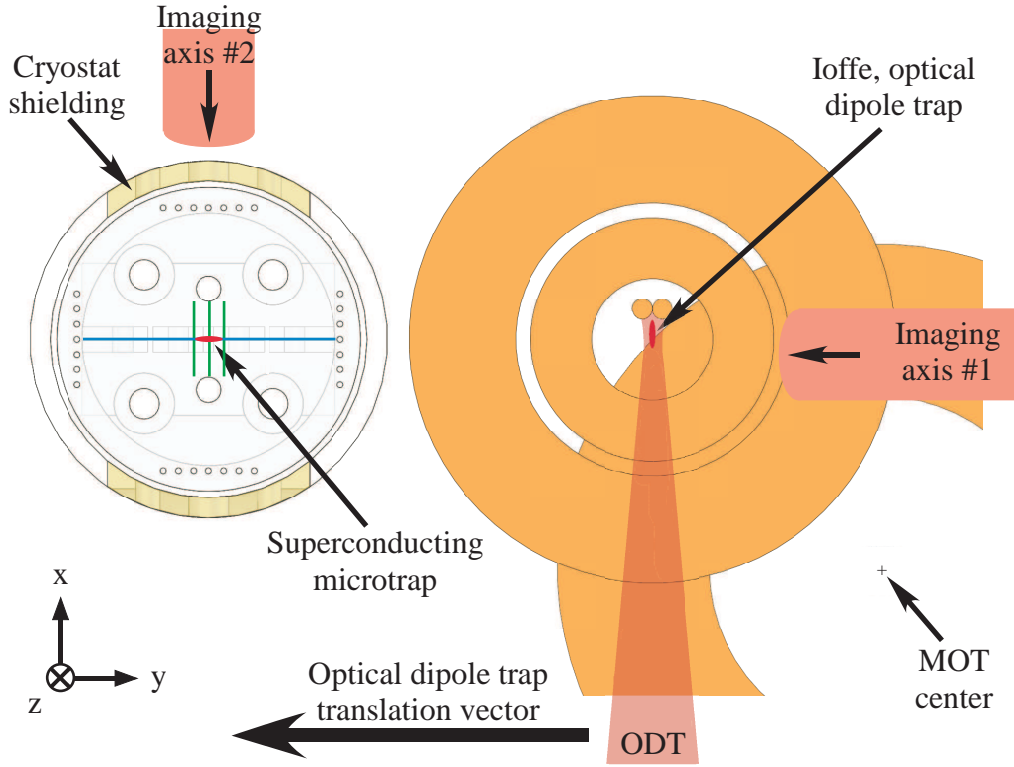


Figure 3.9: View from top showing the imaging axes, and ODT beam before translation to the superconducting microtrap.

when measuring the lifetime near copper.

For imaging path #2, we use an $f = 150$ mm, $D = 50.8$ mm lens, with an image magnification of 1.3. The diffraction limited resolution is $1.22\lambda f/D = 3 \mu\text{m}$. The camera is a SIS1-s285 with an internally cooled CCD chip (1392×1040 , $6.45 \mu\text{m}$ square pixels) to reduce dark counts. Along imaging path #1, a Sony XC-56 (640×480 , $7.4 \mu\text{m}$ square pixels) was used, with a magnification of 2.2 and a diffraction limited resolution of $7.5 \mu\text{m}$.

Three images are taken. The first is an absorption image which produces a shadow depth proportional to the logarithm of the integrated column density of the atomic cloud. The second is an image of the laser field used to illuminate the atoms. The third image is of the background taken when the imaging laser is shut.

In a purely harmonic trap, thermal clouds have a gaussian density profile, with a spatial extent that depends on their temperature and the trap frequency:

$$\sigma_x = \sqrt{k_B T_{\text{cloud}} / m_{Rb87} \omega_x^2} \quad (3.4)$$

Here, σ_x is the standard deviation of the density profile along the x direction. The gaussian FWHM (F) is then $F = 2\sqrt{2 \ln 2} \times \sigma_x$. For a cloud with $T_{\text{cloud}} = 150$ nK, and a radial trapping frequency of $\omega_r/2\pi = 100$ Hz, the cloud size in this direction is of the order $F = 15 \mu\text{m}$. This translates to about 3 pixels in the imaging plane.

In order to better resolve cloud features, images are usually taken in time-of-flight

(TOF) where the cloud is allowed to freely expand for several milliseconds while falling under gravity, before being illuminated with resonant light. In this way, information on the atomic momentum distribution, and hence the cloud temperature is obtained. From two measured FWHMs ($F_{1,2}$) at two different TOFs ($t_{1,2}$), the temperature can be calculated by,

$$T_{cloud} = \frac{C (F_2^2 - F_1^2)}{t_2^2 - t_1^2} \quad (3.5)$$

where $C = m_{Rb87}/8k_B \ln(2)$.

3.7 Experimental timing

In this section we will detail the events of a single typical experimental run during the lifetime measurements. The experimental timing is controlled by an ADwin Pro II. This system has a built-in dedicated 300 MHz processor, and is connected via ethernet to a control computer. On the control computer, the AdwinControl GUI allows to initiate an event sequence, and when necessary to halt execution (there is no pause capability). The event sequences are detailed in self-coded AdwinControl scripts (see Appendix A). Upon loading such a script into AdwinControl, it is possible to change external variable values representing times or voltages before executing the run. This obviates the need for continually updating the code to reflect the most recent experimental parameters, since these can readily be saved and loaded.

The voltage control signals are produced by a single digital card with 32 channels and 2 analog cards with 8 channels each. Voltages can be applied to several channels synchronously, whereas changes on a single channel require a $4 \mu\text{s}$ settling time. Adwin is not able to output large currents, so a current amplifier has been used for devices which draw a current of greater than 5 mA. This is required e.g. to control the AOM driver used for switching the optical tweezers.

To represent the timing of the experiment, we show various relevant parameters (rows) as a function of time. Since several orders of magnitude are present during the preparation of ultracold clouds, the plots are divided vertically into columns which display a certain time window.

Fig. A.1 shows the timing during Sisyphus cooling, optical pumping, and magnetic trap formation phases. The Rb dispenser current (not shown) is applied during the first 14 s to feed the MOT. By monitoring the fluorescence, we observed that the atom number in the MOT peaks several seconds after the dispensers are turned off. To optimize the lifetime in the Ioffe trap, however, a balance must be found between high atom numbers and minimal background pressure. For this reason, the Sisyphus cooling phase begins at 22 s, a few seconds after the MOT reaches peak fluorescence.

Thermal fluctuations of the AOM due to switching the 1.5 W rf input on and off can lead to significant power fluctuations in the first diffraction order, which were seen to

degrade the performance and repeatability of optical pumping. The OP AOM has therefore been left on for the majority of the experimental run in order to maintain thermal equilibrium. The OP AOM extinguishes the beam 10 ms before the OP shutter is opened. Approximately 0.25 s later, the OP AOM is turned on for 80 μ s of optical pumping. Somewhat after the physical OP shutter is closed, and the OP AOM goes on again for the remainder of the experimental run.

Fig. A.2 shows the magnetic transfer process. The starting time here is immediately after atoms are magnetically trapped by the MOT coils. After a 1 s hold time in a static quadrupole trap to allow thermalization, the center of the quadrupole is shifted by 32 mm to be concentric with the transfer and Ioffe coils. This is realized in about 1 s by gradually reducing the MOT coil currents, while increasing the fields created by the transfer and compression coils. The resulting temperature and atom number were found to be stable to moderate changes in the ramping scheme, indicating that the adiabatic condition is easily satisfied. The Ioffe wires are turned on before the end of the transfer process (while the MOT coils are still on) in order to optimize the cloud temperature, and minimize the number of atoms that are lost due to surface spilling. At the very end of the time window depicted in Fig. A.2, the Ioffe trap is static and evaporative cooling begins.

The cloud is evaporatively cooled with a 16 s rf sweep. The frequency as a function of time roughly resembles a negative exponential of the form $\nu(t) = F_0 \times \exp(-t/\tau_c)$, where $\tau_c \approx 6.5$ s is the characteristic $1/e$ time for the frequency, and $F_0 = 12$ MHz is the starting frequency. The actual shape of the curve, however, is crafted from a piecewise optimization of the phase space density, and differs significantly from the negative exponential. In general, the cooling efficiency is less sensitive during the early stages of evaporation, but highly sensitive to variations in the final frequency or ramp time.

The cold cloud is next loaded into an optical tweezers. The procedure is simple, relying on careful alignment rather than careful timing (see Sect. 3.4.3). The Ioffe trap is expanded in 100 ms by slowly ramping off the TR coils which adiabatically cools the cloud. Next the tweezers light is ramped up in 300 ms, after which the Ioffe coils and wires are switched off in 20 ms. Once the cloud is loaded into the ODT, we shift it in 570 ms to the region of the superconducting microtrap (SCMT).

Fig. A.3 depicts the loading procedure into the superconducting niobium wire trap, as well as the subsequent experimental routine. The left column shows the loading. An important point is that the loading current is limited by the resistive heating (at the NC-SC contacts), and must therefore be kept small (< 1.6 A). This puts a cap on the maximum distance from the wire where the cloud can be loaded. Typically we observed better loading efficiency with smaller loading current (here we use 0.73 A). The SCMT is turned on in 1.2 s, at which time the AOM is turned off in 300 ms. Although the mode match is poor, the loading captures %40 of the atoms at about %40 of their initial temperature.

Between the second and first column of Fig. A.3, there is an rf evaporative cooling

stage lasting 8 s. The resulting cloud acts as our probe for the superconducting surface. The second column of the figure shows the experimental procedure for the lifetime measurements near niobium (Sect. 4.2). In order to measure the lifetime, the cloud is moved from the cooling position to an intermediate hold position and allowed to thermalize for 1 s. Then it is moved to a distance d from the niobium surface, and held for a variable time (indicated by a blue stripe), after which it is ramped to a set distance from the surface for time of flight imaging.

Finally, the imaging process uses two physical shutters to allow full extinction, in conjunction with an AOM, which enables the short ($30 \mu\text{s}$) exposure time. One of the physical shutters is in the closed position 2 ms both before and after the start of the exposure. While the shutters are closed, the AOM is left on to keep it thermalized, as with the OP AOM above. Two exposures are required to form and absorption image. These occur 0.5 s from each other due to the camera's limited read out speed of the CCD chip.

Chapter 4

Measurements in the superconducting microtrap

In this section we present the results of measurements in the superconducting microtrap. These measurements demonstrate for the first time the Meissner effect in an atom trap, and trapping lifetimes in excess of the Johnson noise limit at the near-field distances.

4.1 Meissner effect

In this section, we describe measurements of the Meissner effect in the superconducting microtrap. It is shown that, at low temperatures ($T < 6$ K), the cylindrical wire creates a deviation of the trap position with respect to the normal conducting case in perfect agreement with theoretical expectations. As the wire temperature is increased, the Meissner effect weakens allowing partial magnetic field penetration. This is manifested as a decrease in the wire's effective superconducting radius. For a more complete discussion of the topics covered here, see the PhD thesis of Daniel Cano (Can09) and the publication of Cano et al. (Can08a).

To measure the Meissner effect, we begin by loading a cloud into the SCMT using a slightly different loading procedure¹ than that shown in Fig. A.3. The trap is formed by ramping up the trap currents in 100 ms, and then ramping down the AOM power in 300 ms. In this way we load 4×10^5 atoms at $5 \mu\text{K}$ into a trap formed by a niobium current of $I = 1.6$ A, a capping current of $I_{\text{cap-A,C}} = 0.01$ A, an external bias field of $B_x = 6.4$ G, and an offset field of $B_0 = 1$ G. The radial and axial trap frequencies are $\omega_r/2\pi = 160$ Hz, $\omega_a/2\pi = 2$ Hz. Once loaded, the atoms are moved adiabatically to their final position in 0.5 s by reducing the niobium current. After a short hold time, the atomic cloud position is imaged in the trap (without time-of-flight).

¹Although the procedure is not optimal in terms of the phase space density of the captured cloud, this does not have an adverse effect on the cloud position measurements. The loading was subsequently optimized for the lifetime measurements.

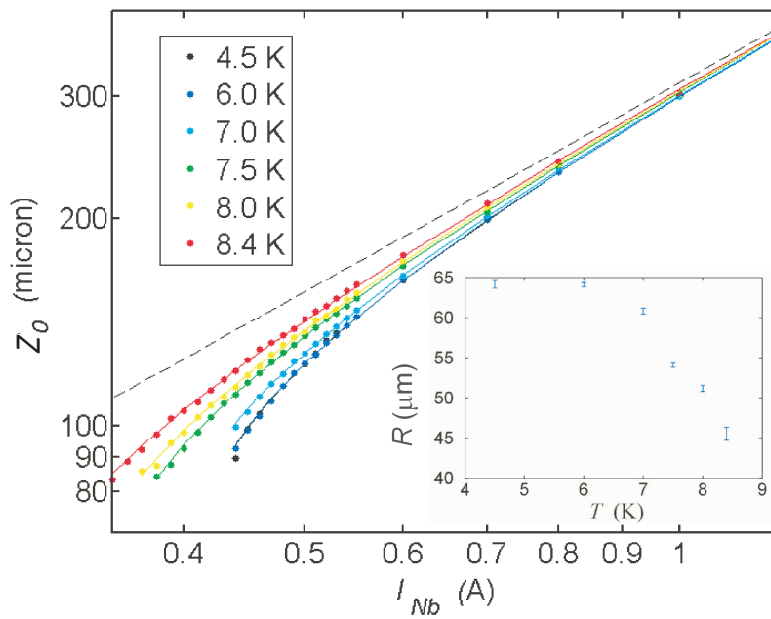


Figure 4.1: The Meissner effect at different cryostat temperatures. Below 6 K the niobium wire is in the pure Meissner state. At higher cryostat temperatures, as flux penetration occurs, the wire trap position more closely resembles that of a normally conducting trap. The inset shows the decrease of the wire’s effective radius, R , as the temperature approaches T_c .

To determine the distance of the cloud to the wire surface for a particular wire current, a fitting procedure is employed. The cloud position is determined by fitting the atomic density profile to Boltzmann's expression for the thermal occupation of levels in a trapping potential $U(z, x) = m_F g_F \mu_B |B| - mgz$. The fit takes into account the effects the linear gravitational potential, which shifts the minimum of the harmonic trap. This gravitational sag is given by (For07),

$$\Delta_g = \frac{g}{\omega_z^2} \quad (4.1)$$

$$= \frac{mgB_0}{m_F g_F \mu_B a_0} \quad (4.2)$$

and is on the order of a couple microns for typical trap parameters. The deviation of the potential from a purely harmonic trap is also accounted for by using a more realistic expression for the magnetic field in the trapping region.

The location of the wire surface can be determined uniquely from the diffraction pattern it imprints on an imaging beam of uniform intensity, I_0 . In particular, the imaging light intensity reaches a maximum of $1.34I_0$ slightly off the wire, whereas the wire surface is located where the intensity is exactly $0.25I_0$ (Hec98).

Fig. 4.1 shows the measured trap position (its distance from the wire *center*) as a function of the niobium wire current at various temperatures. The colored curves are fits to the data using the theoretical expression for the location of the magnetic trap minimum, given in Table 2.1 as,

$$z_{0,SC} = \frac{\mu_0 I}{4\pi B_x} + \sqrt{\left(\frac{\mu_0 I}{4\pi B_x}\right)^2 - R^2} \quad (4.3)$$

When fitting to the data, the wire radius R is held as a free parameter. The value of R which produces the best fit gives the effective radius of the superconducting wire. The effective radius matches the real wire radius until the temperature exceeds 6 K. In the figure, this accounts for the complete overlap of the trap position at 4.5 and 6 K. As the temperature is further increased, the effective radius drops. This suggests that the Meissner effect plays a less prominent role in determining the trap position, which begins to converge with that of a normal trap, shown as a dotted line. The inset shows the effective reduction of the superconducting wire radius as the temperature approaches $T_c \cong 9$ K.

This reduction of the effective radius demonstrates that the edges of the niobium cylinder are no longer able to maintain superconductivity, and permit the entrance of magnetic flux. For a type-II superconductor flux penetration involves the formation of vortices in the mixed state. The exact nature of the flux penetration is not entirely clear. At these temperatures and magnetic fields, there should be only relatively small changes to the London penetration depth for pure bulk niobium. Specifically, the penetration depth scales with temperature as $\lambda_L(T) = \lambda_0 [1 - (T/T_c)^4]^{-1/2}$, while the critical magnetic fields goes as $B_{c1} = B_{c1}(0) [1 - (T/T_c)^2]$, where $B_{c1}(0)$ is on the order 2000 Gauss for niobium

(Cas05)). This suggests the presence of impurities within the metal, which significantly affect its superconducting properties.

4.2 Spin coherence lifetime

In this section we present measurements of the trap lifetime for an ultracold cloud held in the near field of a low temperature superconductor. Here we detail the first observation of cloud lifetimes in excess of the limit imposed by Johnson noise in normal conducting traps (Kas10).

4.2.1 Lifetime measurements

Lifetime measurements obtained at different distances to the niobium (copper) surface consist of measuring the atom number, N , as a function of hold time, t_{hold} . The resulting decay is fit to a decay function given by,

$$N(t_{hold}) = (N_0 \cdot \exp(-t_{hold}/\tau_1) + N_1) \cdot \exp(-t_{hold}/\tau_2) \quad (4.4)$$

This equation reflects the experimental observation that the atom number decays according to a double exponential. Bringing the thermal atom cloud close to the surface leads to a truncation of the Gaussian density profile. The subsequent surface evaporation and rethermalization (Har03) reduces the number of atoms on a time scale of $1/\Gamma_1$ to typically 5×10^4 and the temperature to 50 nK (Fig. 4.2). The initial atom number is $N_0 + N_1$, with N_1 the asymptotic atom number after surface evaporation. For hold times longer than τ_1 , the atom number decays exponentially on the time scale τ_2 , which contains all experimentally relevant loss mechanisms, such as vacuum background collisions and spin decoherence. We interpret this longer of the two decay times, τ_2 , as the trap lifetime. It should be noted that beyond a certain distance (which depends on the cloud temperature), no initial evaporation is observed. Far from the surface, in the limit $\tau_1 \rightarrow \infty$, we determine τ_2 by fitting to a single exponential. The trap lifetime and the associated loss rate are inversely related by $\gamma = 1/\tau$, and are often used interchangeably.

In the rate picture, Γ_2 represents a direct sum of all loss rates that contribute to the atom number decay at long hold times. The loss rate due to Johnson noise, therefore, cannot exceed Γ_2 .

4.2.2 Niobium measurements

For our niobium measurements, we use the following experimental sequence. The ^{87}Rb atom cloud is loaded into a magnetic microtrap near the superconducting niobium wire. The trap has radial frequency $\omega_r/2\pi = 135$ Hz, axial frequency $\omega_a/2\pi = 4$ Hz. The Larmor frequency is $\omega_L/2\pi = 1.71$ MHz for the spin polarized hyperfine state $|F = 2, m_F = 2\rangle$ at $B_{off} = 2.44$ G. The cloud is cooled by forced evaporation for 11 s, whereby the temperature

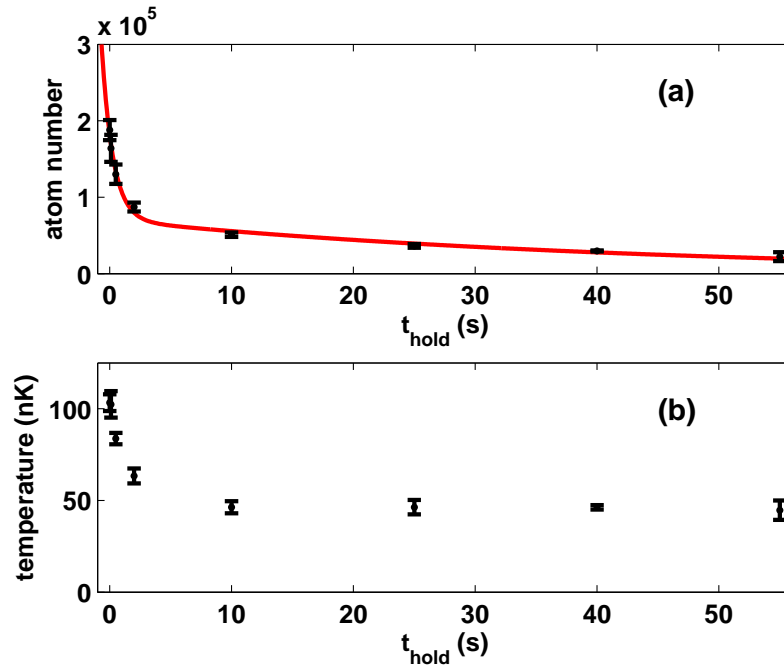


Figure 4.2: Atom number (a) and temperature (b) as a function of hold time for a cloud at 150 nK at a distance of $25 \mu\text{m}$ from niobium. The reduction of the cloud temperature indicates surface evaporation. The fit function (solid red) for the atom number is a double exponential, $N(t_{\text{hold}}) = N_0 \exp(-t_{\text{hold}}/(\tau_1 + \tau_2)) + N_1 \exp(-t_{\text{hold}}/\tau_2)$.

and atom number are reduced to $T \approx 100$ nK and $N \approx 2 \times 10^5$, respectively. The atom cloud is then moved in 1 s to a distance d_{Nb} from the niobium surface (figure 4.6) and held there for a variable hold time t_{hold} . During the shift toward the surface the trap geometry changes: the Meissner effect reduces the radial frequency in our trap geometry. The offset field, which is the only critical parameter for spin decoherence, is kept constant. After the hold time t_{hold} the cloud is shifted away from the surface within 200 ms after which the trap is turned off and the atoms are counted by absorption imaging after 5 ms time-of-flight.

Niobium in the superconducting state is not expected to limit the cloud lifetime in any measurable way. Johnson noise, though technically not completely absent at finite temperature, is strongly suppressed within the superconductor. A simple intuitive argument is that Johnson noise suppression may be attributed to Cooper pairing, whereby each electron is partnered with an electron of equal and opposite momentum. To first order, fluctuations in the current involving Cooper paired electrons average out. Alternatively, in a dissipation free superconductor, the fluctuation-dissipation theorem no longer necessitates the presence of noise power. To show that a superconductor does not emit radio frequency noise associated with fluctuating currents, we must show that the measured loss rate is less than the expected loss rate due to Johnson noise. In principle, one such measurement is sufficient, providing a counter-example to the hypothesis: Johnson noise limits the lifetime near a superconductor. Here we present such a counter-example. The measurements demonstrate for the first time that a superconducting microtrap beats the Johnson-noise limit.

Fig. 4.3 shows the measured loss rate near both superconducting niobium (blue circles) and normally conducting copper (grey points) at 4.2 K as a function of the atom-surface separation. The dash-dotted line (black) is the Johnson noise loss rate near normal conducting copper at 4.2 K calculated from Eq. 2.57 including the measured vacuum background loss (black dotted line). The data below the Johnson noise limit give evidence that magnetic field noise near superconductors is reduced compared with normal metals. Comparison measurements near copper fall above the Johnson noise curve.

In Fig. 4.4, we show a comparison plot of the approximate lifetimes (without the error bars) in dependence of distance near a superconductor from our experiment (Tübingen), near a normal conductor at 4 K (Paris) (Emm09) and at 300 K (JILA) (Har03). The respective Larmor frequencies for these three data sets are (Tübingen, Paris, JILA) $\omega_L/2\pi = (1.7, 1.8, 2.2)$ MHz, whereas the background vacuum lifetimes are roughly (160, 400, 120) s. The experimental conditions are not identical, nonetheless, meaningful comparisons can be made. The three theory curves each use Eq. 2.57, and include the effective lifetime reduction caused by the background vacuum. The red curve is for a conductor at 300 K, while the green and blue curves are each for 4 K but with a background vacuum values of 400 and 160 s, respectively. The niobium data (black) should be compared with the blue curve, however the two are only expected to match in the presence of Johnson noise. We

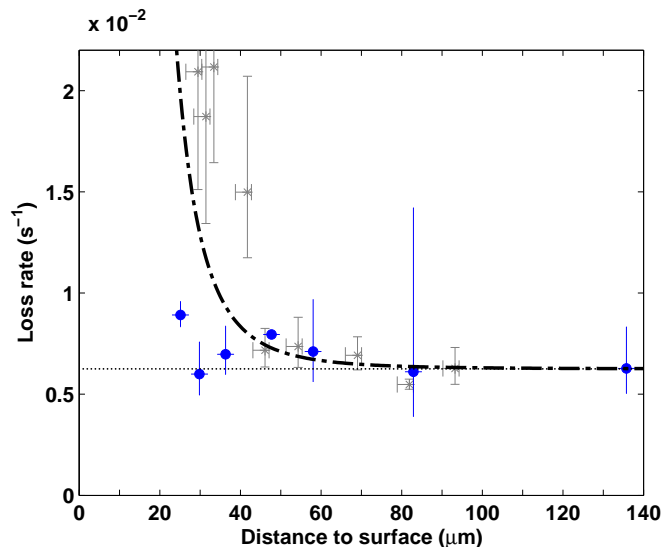


Figure 4.3: Atom loss rate near superconducting niobium at 4.2 K (blue circles) as a function of the atom-surface separation. The dash-dotted line (black) is the Johnson noise loss rate near normal conducting copper at 4.2 K (see Eq. 2.57) including the measured vacuum background loss (black dotted line). The data below the Johnson noise limit give evidence that magnetic field noise near superconductors is reduced compared with normal metals. A comparison measurement near copper is shown by the grey data points.

see that at high temperatures, the theoretical lifetime (red curve) no longer matches the measured values. In this case, better agreement is obtained by a numerical integration of Eq. 22 from Henkel et al. (Hen99).

The advantage gained by simply cooling the conductors is quite clear. The lifetime at $35 \mu\text{m}$, for instance, increases by an order of magnitude. However even at these low temperatures, the lifetime near a normal conductors is fundamentally limited by Johnson noise. The advantage conferred by the use of superconductors becomes apparent at distances below $30 \mu\text{m}$. Most dramatically, at $24 \mu\text{m}$ the superconducting niobium lifetime is 6 times the measured copper lifetime. From the figure it is clear that there are losses within $30 \mu\text{m}$ even for the niobium. These losses have been traced to the the deformation of the trap parameters, which become exacerbated at such distances.

In Sect. 2.1 it was shown how the Meissner effect, characterized by the radius of the wire (Can08a; Can08b; Dik09), plays a significant role in the atom loss within $30 \mu\text{m}$ by changing the trap parameters. Primarily, it reduces the trap depth and magnetic field gradient, while altering the radial oscillation frequencies, ω_r . Closer than $(\sqrt{3} - 1)R$ from the wire surface, the radial trap frequency drops, eventually allowing the cloud to evaporate or spill onto the wire. The influence of the Meissner effect hinders approaching the wire closer than about $20 \mu\text{m}$. There, the initial evaporation phase removes more than 90% of the atom cloud, leading to a strongly reduced signal to noise ratio in absorption

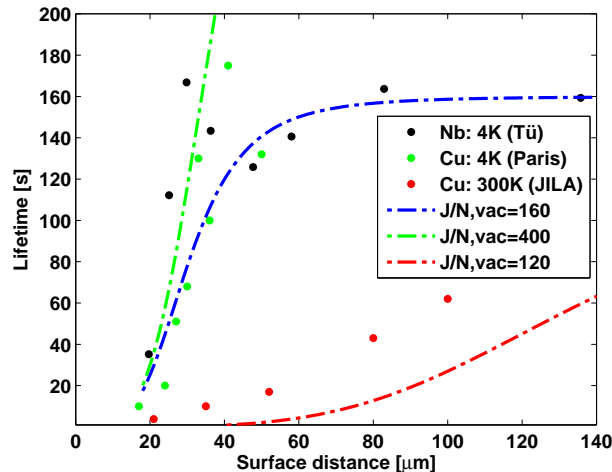


Figure 4.4: Lifetime comparison from three different experimental setups (Tübingen, Paris, and JILA). The black dots represent our data for the estimated lifetimes near a superconductor. Green dots show published lifetimes near copper at 4 K (Emm09), whereas red dots show data near copper at 300 K (Har03). The theory curves use experimental values for the Larmor frequency and background vacuum. The blue curve corresponds to the expected Johnson noise limited lifetime with our experimental parameters

images. In principle, a linear up-scaling of the fields should lead to higher trap depths. However in practice, the loss rate was observed to increase. This is thought to have been the result of parametric heating associated with mechanical vibrations of the trap at some multiple of the trap frequency.

4.2.3 Niobium distance calibration

As discussed in Sect. 4.1, in-situ absorption images perpendicular to the wire measure not only the cloud position, but also the characteristic diffraction pattern from the wire and hence position of the wire surface. This enables an accurate cloud-surface distance to be obtained. This can be extended to arbitrary distance by creating a fit to the theoretical trap position with the bias field as a free parameter. The resulting calibration allows us to obtain the position for arbitrary niobium current to within $\pm 2 \mu\text{m}$.

4.2.4 Copper measurements

Nearby to the free-standing section of the niobium wire, there is copper clamp used for fixing the niobium wire position. The clamp is made of bulk OFHC copper and can therefore be used as a reference material for measurements of the normal conducting lifetime. The results are plotted in Fig. 4.5. Here we see the copper data, and two curves based on calculation. The blue dot-dashed line is the same as in Fig. 4.4, i.e. the Johnson-noise induced spin-flip lifetime prediction for copper at 4K, together with a constant

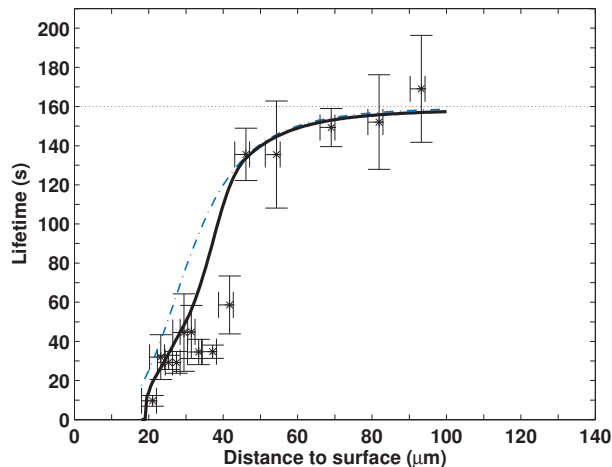


Figure 4.5: Lifetimes measured near normally conducting copper. The cloud temperature is 300 nK. The dot-dashed line (blue) indicates theoretical predictions for the lifetime considering Johnson noise and a background vacuum of 160 s. For the solid line (black), evaporation is added and this accounts for an additional lifetime drop, especially within of 40 μm the surface.

vacuum background decay time of 160 s.

For copper, we use a different trap configuration than for the niobium measurements, with frequencies $\omega_r/2\pi = 138$ Hz, and $\omega_a/2\pi = 21$ Hz. The axial offset field is kept at the same value as in the copper measurements. After evaporative cooling to $T \approx 300$ nK and $N \approx 2 \times 10^5$, the cloud is moved toward the copper, whereby surface cooling leads to a minimum temperature of $T \approx 150$ nK with $N \approx 5 \times 10^4$ atoms.

4.2.5 Copper distance calibration

To bring the atomic cloud closer to the copper surface, the external bias field is rotated about the wire axis while keeping the current in the niobium wire constant (see Fig. 4.6). As the magnetic field along B_z is increased linearly, the field along B_x is decreased so as to keep the modulus of the field nearly constant. The trap minimum is moved on a circle around the center of the wire, with the angle of the deflection given by the ratio of vertical and horizontal magnetic fields, $\alpha = \arctan(B_z/B_x)$. The distance of the atomic cloud to the copper surface is determined by the projection of the trajectory on the z-direction,

$$d = r(B) \cos \alpha - z_0 + \Delta_g, \quad (4.5)$$

where $r(B)$ represents the distance from the cloud center to the niobium wire center as a function of the the magnetic field modulus, $B = \sqrt{B_x^2 + B_z^2}$. The height difference between the copper surface and the wire center is z_0 , and Δ_g is the gravitational sag (Eq. 4.1).

Close to the copper surface, for angles greater than 60 degrees, the atomic cloud cannot be imaged. The above function is fit to the position measurements up to 60 degrees.

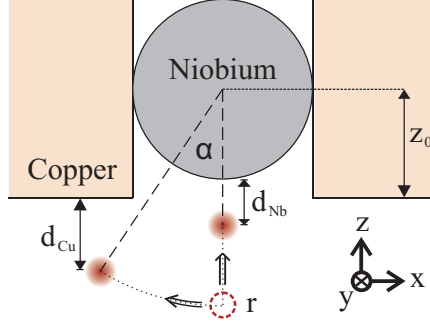


Figure 4.6: Schematic view along the wire of the approach to copper and niobium. From an initial position (open dashed circle) at $r=250\ \mu\text{m}$, $\alpha=0^\circ$, the cloud is moved closer to the niobium wire at constant α , or at constant r toward the copper surface, reaching a final distance of d_{Nb} or d_{Cu} .

Increasing the vertical field further eventually leads to surface evaporation. By determining the exact fields at which the trap coincides with the surface, the distance to the copper surface is calibrated as a function of B_z . By quickly ramping up and down the vertical field, we measure the atom number vs. distance and choose the value corresponding to when all atoms are lost. This assumes that the trap remains in the vicinity of the surface long enough that all atoms can reach the wall. In our case, this approximation introduces an error in the distance calibration. Additional sources of error result from the cloud climbing the potential wall as the approaching trap is suddenly reversed, and from the attractive Casimir-Polder potential which dominates the magnetic potential at a distance of $1\ \mu\text{m}$ from the surface. The total error of the calibration, including statistical error due to shot-to-shot variation in the measured cloud position, is $-3/ + 1\ \mu\text{m}$.

4.2.6 Trap lifetime: contributing factors

The lifetime of an atomic cloud in a magnetic trap is limited by a number of factors. Collisions can, in general, lead to heating and atom loss. The room temperature background gas sets a limit on the trap lifetime which is independent of the cloud density (see Sect. 3.1.4). Within the cold cloud, two-body and three-body processes can occur leading to spin relaxation, or molecule formation (Wei03b), respectively. The loss rates are density dependent, and we work with low densities ($\approx 10^{-12}\ \text{cm}^{-3}$) so as to minimize their impact.

Majorana losses, which occur when an atom cannot adiabatically follow the magnetic field, are another significant source of loss in traps that lack a sufficiently smooth magnetic minimum. However, for an ultracold cloud in a Ioffe trap, this effect is expected to be negligible.

Perhaps of greatest concern is technical noise. Early on, rf noise emitted from the translation stage controller was found to couple to the mains voltage, leading to a drastic reduction of the lifetime to $\approx 1\ \text{s}$ at $25\ \mu\text{m}$. Once this issue was resolved, we were

able to measure two orders of magnitude longer lifetimes. Nonetheless, an unexpected dependence of the cloud lifetime on the Larmor frequency indicates that some residual rf noise persisted. The presence of a surface introduces two additional loss processes, namely Johnson noise and surface evaporation. The role of Johnson noise has been discussed in detail in Ch. 2. Additionally, measurements of the Johnson noise limited lifetime in a cryogenic environment near normally conducting copper have been performed by Emmert et. al (Emm09). We shall now cover the topic of surface evaporation.

4.2.7 Surface evaporation

Surface evaporation is a leading concern in the cylindrical wire trap due to the Meissner effect. The resulting opening of the trap onto the surface makes this the dominant loss mechanism. Although it reduces the lifetime near the surface, it can also be used to cool the cloud evaporatively. Radio frequency cooling is most common, but surface evaporation has been used to create a BEC with similar efficiency (Har03).

In order to understand the role of surface evaporation, we have implemented a simple model which nonetheless provides reasonably good agreement with measured lifetimes for copper and niobium. Detailed evaporative cooling models assume the cloud is in quasi-equilibrium, and maintains a truncated Gaussian profile (Lui96). For our purpose, it is sufficient to assume that the wire introduces a spatial cutoff, which translates to an energy cutoff under the ergodic assumption. The real trap shape which results from considering the Meissner effect has been taken into account. For time steps shorter than the thermalization time, we suppose that the cloud exponentially approaches the new temperature, determined from the average energy of the lost particles and including a heating rate. The experimentally measured heating rate is less than 5 nK/s. We approximate the loss mechanism as a linear process within one trap oscillation period, allowing arbitrarily short time steps to be chosen. The lifetime reduction due to evaporation near the copper surface is shown in Fig. 4.5. Within 20 μm , the cloud is lost before it can thermalize to a lower temperature. Beyond 20 μm , the cloud undergoes evaporation, and the lifetime rises sharply. The finite heating, though small, clearly reduces the lifetimes observed especially at low trap depth, where it maps directly to atom loss. It generates significant losses over long hold times considered, reducing the slope until 30 μm . Further than this, only a small fraction of atoms can collide with the wall even at long hold times.

Chapter 5

Conclusion

In this thesis, I have presented the details of an experiment demonstrating for the first time the absence of Johnson-noise-limited trap lifetimes for an atomic cloud in close proximity to a conducting metal. The experiment, which we designed and built for this purpose, consists of a combination of techniques from experimental atomic, and low temperature solid-state physics. On the atomic physics side, we have implemented a setup using the now standard techniques of laser, and evaporative cooling. This allows us to prepare ultracold atomic clouds, which subsequently act as sensitive probes of the magnetic field at radio frequencies. Physically (and thermally) separated from this apparatus, a helium flow cryostat was used to cool a niobium wire to less than 4 K, bringing into reach the realm of low temperature superconductivity, and thereby enabling investigation into this solid-state phenomenon. To bring the atoms to the region of the superconducting microtrap, the focusing lens of a optical tweezers, mounted upon a floating translation stage, was moved in a highly controlled motion.

Once loaded into the superconducting trap, we have carried out investigations into the Meissner effect, finding that it distorts the trapping potential in a way which is highly dependent on the wire geometry. By examining the temperature dependence of this distortion, it was found that the effective radius of the wire decreases as the temperature rises above about $2/3$ the transition temperature, indicating magnetic field penetration into the superconductor.

Measurements of the lifetime of atomic clouds as a function of distance to the superconductor revealed no noticeable losses resulting from fluctuating currents within the metal. Despite a strong reduction of the trap depth toward the surface, we were able to measure lifetimes in excess of the expected Johnson-noise-limited lifetime of a cloud near a copper surface at the same temperature (Kas10). This is direct evidence for the suppression Johnson noise in a superconductor. This result was anticipated on theoretical grounds due to the effects of electromagnetic screening, and the inability to deposit energy into a superconductor below the energy gap. However observation of the expected orders of magnitude increase to the atomic lifetime is currently technically unrealistic. Improving

the background vacuum and optimizing the wire geometry are realistic steps which can be taken along these lines.

In future experiments with superconducting atom chips, interesting phenomena may be explored. A short term goal would be to discover the signature for the onset of vortex creation in niobium thin-films. When pinned, vortices will lead to a static alteration of the magnetic field profile. However, even more intriguing is the possibility of investigating time dependent phenomena, such as vortex flow in a transverse magnetic field. For this, it would be necessary to implement a non-destructive continuous imaging system, such as phase-contrast imaging. Furthermore, it would be highly beneficial to decouple the trapping elements from the sample to be measured. Optical traps would be ideal, however it is unclear how an optical trap could be used to bring atoms to within microns of a surface, especially without introducing unwanted effects (such as heating of the substrate). Scheel et al. (Sch07) have suggested observing the Kosterlitz-Thouless transition in superconducting thin films by observing dephasing of the Zeeman sublevels by Ramsey interferometry.

Along the lines of device physics, one can envision many fascinating possibilities. One simple idea is to use the persistent current of superconducting loop (Muk07) to realize an atom interferometer (Mue08). But considerably richer physics becomes accessible with the introduction of coherent devices to the atom chip. It is well known that a Josephson junction provides an extremely stable voltage to frequency conversion at approximately 483 THz/V. By integrating such a device onto an atom chip, it may be possible to address transitions between rubidium groundstate hyperfine levels at 5.8 GHz.

Josephson junctions are also a key component in superconducting quantum interference devices (SQUIDs). The detection of the magnetic moment of a spin-polarized atom cloud with a dc-SQUID appears difficult but feasible. The appeal of this detection method is that it is non-destructive, and does not require optical access. Large condensates are desirable since a single atom generates less than 10^{-9} flux quanta through a micron-sized loop at one micron distance. Ultimately ac-SQUIDS may also be employed. Such a device could be used to detect Rabi-oscillations between two hyperfine states via lock-in techniques.

M. Singh proposed generating quantum entanglement between a BEC and the quantized flux states of a superconducting loop. Conceptually, this is one of the more elegant proposed methods for creating BEC entanglement (Sin09). Technologically, however it shall prove extremely challenging due to the utter fragility of entangled "cat" states. The idea is to prepare a rf-SQUID in a macroscopic superposition of flux states. Indirect evidence for this type of macroscopic coherent superposition has been demonstrated experimentally by the observation of a coherent tunneling resonance between flux states (Wal00; Fri00). For the sake of argument, let us suppose such a state can be formed. Then, since each flux state creates a distinct magnetic potential for the atoms, the superposition of flux states creates superposed magnetic traps. Measuring which trap the cloud occupies forces the SQUID loop to collapse to the corresponding flux orientation. Given

the weak atom-surface back action, and the huge number of cooper pairs involved in such a state, this is indeed remarkable! Alternatively, for a BEC, interferometric measurement would allow a sort of state tomography of the loop, with distinct results for a coherent macroscopic superposition of flux states, and an incoherent mixture.

A highly sought-after goal is the creation of a strong atom-surface coupling. For this purpose it has been suggested to use an on-chip coplanar waveguide resonator (Pet08; Pet09) coupling to an ensemble of Rydberg atoms. Applications include quantum information processing utilizing the coherent exchange of information between a solid-state and cold atom systems. Such hybrid systems have significant potential. In this case, the cold atoms with long coherence times could be used as quantum memory for a solid state circuit. The goal is to combine the considerable know-how of the solid state and atomic physics communities to further both fields.

Appendix A

Computer control

Here we describe the AdwinControl and Matlab code used to run the experiment and streamline subsequent analysis.

A.1 ADwinControl

The Adwin system is used to control or trigger each event of the experimental cycle, from shutters and coils to the translation stage. The sequence of events is coded via the AdwinControl programming language. It is based on the low-level language ADBASIC. With relatively few commands, the voltage of a certain channel can be set with microsecond time resolution. Fortunately conditionals, and even some mathematical operations, with capabilities similar to a scientific calculator are possible within the code. Looping variable values can be implemented intrinsically within a single run, but it was not possible to have a set of variables cycle from run to run between values in an automatic and readily controllable manner. However there is a work-around described in A.3.2.

In order to run the experiment in a continuous loop, we create an AdwinControl Macro (*.acm) file with the following commands:

```
#REPEAT ON  
_RUNTIME(run)
```

where `run` is a user defined variable which determines the lower bound on the run time.¹ This is the standard way to run an experiment and allows the external variables (see below) to be modified by the user, with the changes occurring at the beginning of the following run.

The variable `run`, is defined in our code, along with the other user-accessible variables, by including an AdwinControl Include (*.aci) file

```
#INCLUDE [path]\Modules\External\External_variables.aci
```

¹Note: if an event takes place after the allotted runtime, it automatically extends until the last event.

Note that throughout this appendix, the string `[path]` *must* be replaced by the valid folder path string in order to obtain valid code. In our case the `[path]` string is,

```
C:\Dokumente und Einstellungen\Labor\Desktop\ADwinControl\SCMT Labor
```

Include files act as though they were manually inserted into the code. This particular file contains all our `#EXTERNAL` variables (which may also be inserted manually anywhere in the code). Variables defined as `#EXTERNAL` can be changed by the user from one run to the next through the external variable graphical user interface (EV-GUI). Loading the variable values into the EV-GUI allows them to be changed by the user. The changes appear in red and must be certified, after which they appear in yellow. After the code is compiled and sent to the hardware at the beginning of the run, the values appear in green.

Beside `#EXTERNAL`, the other variable definitions are `#STATIC`, or `#GLOBAL`. The `#STATIC` variables are internal. Declaring a variable as `#GLOBAL` writes its value to a comma-separated variable (*.csv) as long as the following line is uncommented:

```
#PROJECT proj_name
```

and appears before the experimental loop. All globally declared variables are then written to `'proj_name.csv'`. The output can also generate a complete copy of the code that was sent to the compiler, allowing a full reconstruction of each run.

The backbone of the experimental procedure, which we call main program is as follows:

```
#INCLUDE [path]\Modules\External\Global_variables.aci
#INCLUDE [path]\Modules\External\External_variables.aci
#INCLUDE [path]\Delays.aci
#INCLUDE [path]\Channel_Assignment.aci
#INCLUDE [path]\Channel_Config.aci
// Record code and global variables
#PROJECT Copper
#REPEAT ON
// %%%%%%%%%%%%%%%%%%%%%%%%%%%%%%%%%%%%%%%%%%%%%%%%%%%%%%%%%%%%%%%%%%%%%%%%%
// BEGINNING OF MAIN PROGRAM LOOP
// %%%%%%%%%%%%%%%%%%%%%%%%%%%%%%%%%%%%%%%%%%%%%%%%%%%%%%%%%%%%%%%%%%%%%%%%%
_RUNTIME(run)
T=0
DSET(1, AdwinTrigger, TriggerZeit, 1)
#INCLUDE [path]\Modules\Inow.aci
IF(AUTO_ON)
    #INCLUDE [path]\Modules\Auto\Auto_auto.aci
ENDIF
// also contains Sisyphus and OP
#INCLUDE [path]\Modules\MOT_ON.aci
```

```

IF(MAG_TRAP_y1n0)
    #INCLUDE [path]\Modules\Mag_trap.aci
ENDIF
IF(Ioffe_Trap_y1n0)
    // FIRST trigger for TR stage (MOT pass -> collection region)
    DSET(1, TR_StageTrigger, T, 1)
    DSET(1, TR_StageTrigger, T + 50ms, 0)
    #INCLUDE [path]\Modules\TR_QPtrap.aci
    // EVAPORATIVE COOLING
    // 0 - no cooling // 1 - cool to BEC // 2 - cool to thermal cloud
    IF(freq_ramp_select)
        #INCLUDE [path]\Modules\freq_ramp.aci
    ENDIF
    // hold time in Ioffe trap (after cooling) for lifetime comparison
    T = T + Ioffe_hold
    IF(Optical_dipole_trap_y1n0)
        #INCLUDE [path]\Modules\DipoleTrap.aci
    ELSE
        // Target atoms with resonant light (and trigger the TR stage)
        #INCLUDE [path]\Modules\TargetAtoms.aci
    ENDIF
ELSE
    #INCLUDE [path]\Modules\currents_off.aci
    #INCLUDE [path]\Modules\Imaging.aci
ENDIF
// End of experimental run
#INCLUDE [path]\Modules\collectMOT.aci

```

Note that the variable T is regularly updated and loosely represents the 'current time' in microseconds during and experimental run.

A.2 Experimental timing plots

Here we present plots of critical aspects of the experimental timing. In each plots, adjacent columns can have different time axes. In this way we can represent details which occur on significantly different time scales. The experimental timing of the Sisyphus, optical pumping and magnetic trap formation is shown in Fig. A.1. The magnetic transfer from the MOT region into an Ioffe trap is shown in Fig. A.2. Finally, the procedure for loading the superconducting wire trap from the optical tweezers beam is shown in Fig. A.3.

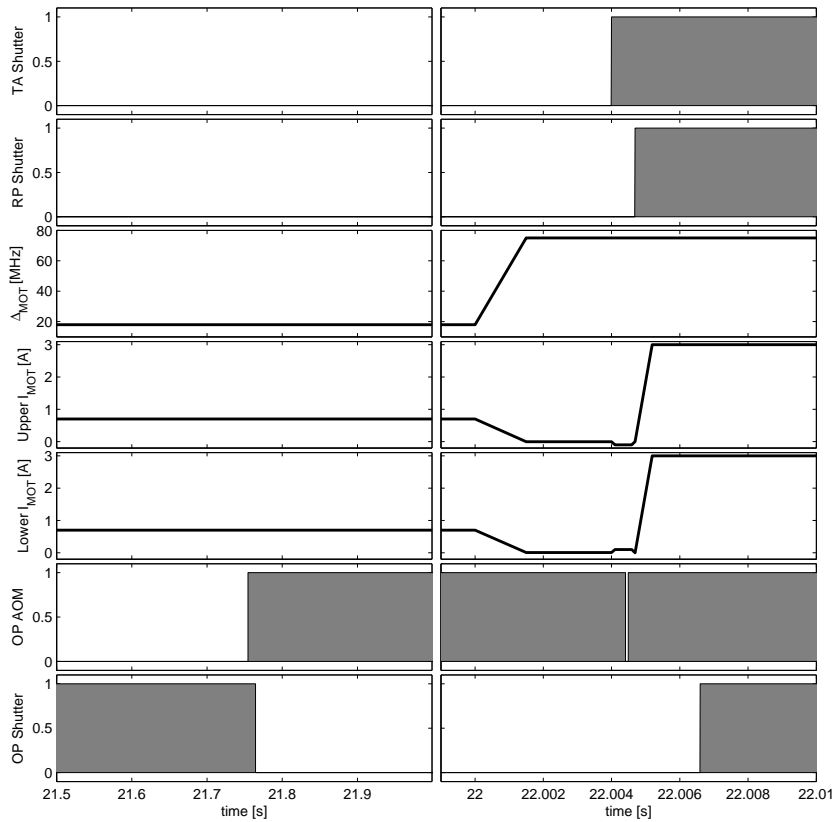


Figure A.1: Experimental timing: Sisyphus, optical pumping and magnetic trap formation phases. Columns represent a single time window. Rows display the values for the experimental parameters. Positive current in both MOT coils represents the anti-Helmholtz configuration. At 22 s, the Sisyphus cooling begins. The MOT coils apply a small Helmholtz field to compensate the earth's field, while the MOT detuning is increased from 18 MHz to 75 MHz. After 2.5 ms of status, the TA shutter closes, and optical pumping begins. The Helmholtz field is increased, and the OP AOM (fast shutter) opens for $80\mu\text{s}$ (seen as a thin white stripe in the plot on the right). Subsequently, the OP, and RP shutters are closed, and the MOT coils return to anti-Helmholtz to capture the spin polarized cloud with 3A of current.

A.2. Experimental timing plots

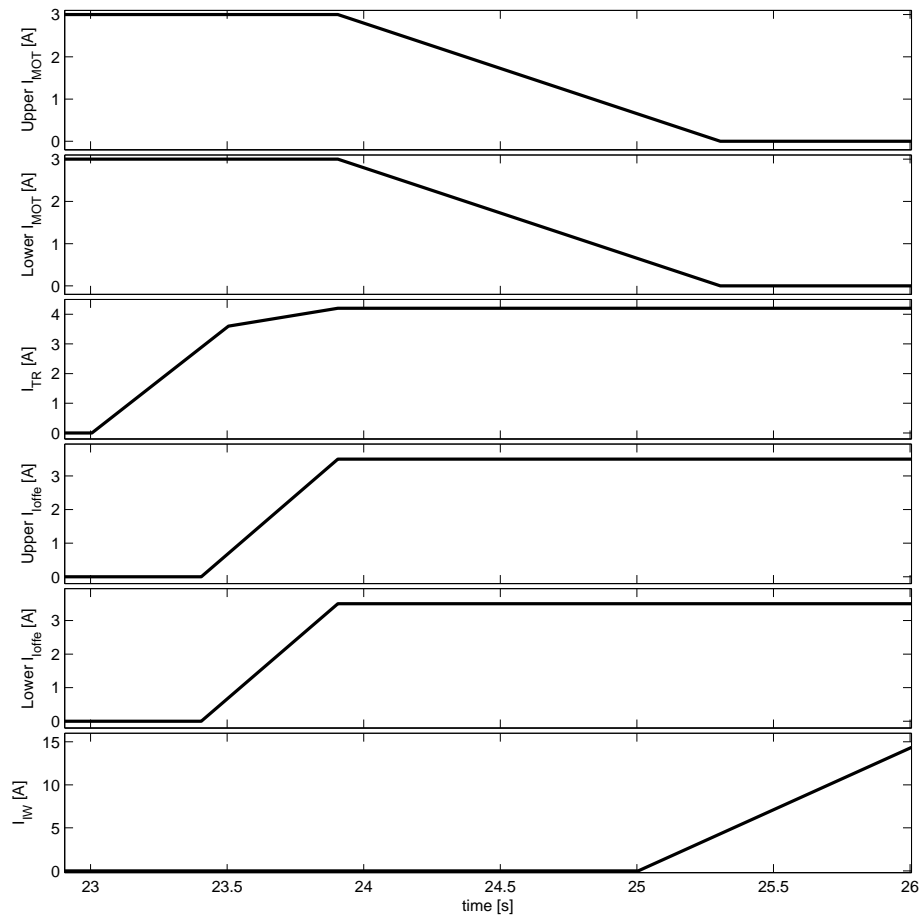


Figure A.2: Experimental timing: magnetic transfer. From a magnetic trap formed by the MOT coils, the cloud is transferred to a Ioffe trap by ramping up the TR and Ioffe coil currents, as well as an Ioffe wire pair, while ramping down the MOT coils.

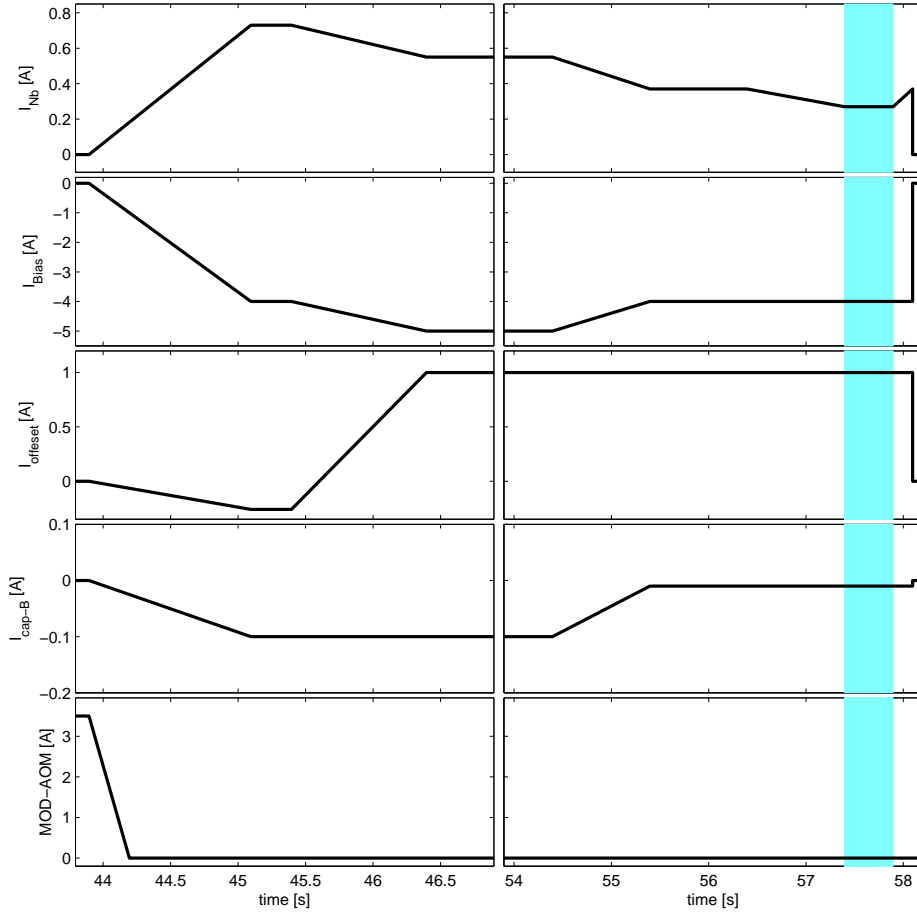


Figure A.3: Experimental timing: loading from the ODT into the SCMT (*left*). Typical parameters during operation of the SCMT are shown in the second column (*right*). The atom number is measured after a variable hold time of t_{hold} (shown as a blue vertical stripe) near the niobium surface. An additional pair of "capping" wires ($I_{cap-A,C}$ not shown), running parallel to I_{cap-B} are used to improve the field configuration during the loading, cooling (with $I_{cap-A,C} = 0.2$ A) and holding (with $I_{cap-A,C} = 0.1$ A).

A.3 Matlab

In this section, I will present Matlab code used for a range of applications. These include magnetic field simulations, automatic Adwin script generation for cycling experimental variable inputs, and a graphical user interface (GUI) for efficiently analyzing an extensive data set.

A.3.1 Magnetic field simulations

We calculate the magnetic field at an array of points in a (user-specified) 3D region of space for an given arrangement of coils and wires. The geometry is used to calculate the magnetic field per amp of current for each of the elements. This information is stored in a '*.mat' file, which can be accessed and scaled accordingly. The field calculation is then viewed as a "one time cost" computationally, after which only a linear scaling and summing is involved to find the total fields. Time evolution of the fields as a function of the component currents can thus be evaluated readily. Here we reproduce the code for calculating the field of a current loop using elliptic integrals. Coils are approximated by an array of current loops.

```
%%%%%%%%%%%%%%%%%%%%%%%%%%%%%%%%%%%%%%%%%%%%%%%%%%%%%%%%%%%%%%%%%%%%%%%%
%%%- Magnetic field of a unit current loop -%%
%%%%%%%%%%%%%%%%%%%%%%%%%%%%%%%%%%%%%%%%%%%%%%%%%%%%%%%%%%%%%%%%%%%%%%%%
%% Brian Kasch
%% July, 2005. University of Tübingen.
%%%%%%%%%%%%%%%%%%%%%%%%%%%%%%%%%%%%%%%%%%%%%%%%%%%%%%%%%%%%%%%%%%%%%%%%
%% For methodology: see
%% http://www.netdenizen.com/emagnetest/offaxis/?offaxisloop
%%%%%%%%%%%%%%%%%%%%%%%%%%%%%%%%%%%%%%%%%%%%%%%%%%%%%%%%%%%%%%%%%%%%%%%%
%% This program calculates the magnetic field in S.I. units. of a
%% circular current (I=1A) loop using elliptical integrals in a
%% region of space determined by x,y,z.
%%%%%%%%%%%%%%%%%%%%%%%%%%%%%%%%%%%%%%%%%%%%%%%%%%%%%%%%%%%%%%%%%%%%%%%%
%% INPUT %%
%% center: Vector determining the loop center.
%% d: Vector determining the direction of the loop axis (normalized
%%     below).
%% radius: Loop radius.
%% x,y,z: e.g. linspace(-5,5,11),linspace(-1,1,21),[-1 0 1].
%%       Must be vectors (or scalars). meshgrid converts to arrays.
%%%%%%%%%%%%%%%%%%%%%%%%%%%%%%%%%%%%%%%%%%%%%%%%%%%%%%%%%%%%%%%%%%%%%%%%
%% OUTPUT %%
%% B_x (resp. B_y, B_z): for the above choice of x,y,z:
```

```

%%      (21,11,3) array with values of B_x (resp. B_y, B_z) at the
%%      corresponding Xgrid,Ygrid,Zgrid positions.
%%%%%%%%%%%%%%%%%%%%%%%%%%%%%%%%%%%%%%%%%%%%%%%%%%%%%%%%%%%%%%%%%%%%%%%%
%% USAGE E.G. %%
%% [B_x,B_y,B_z]=unitcurrent_loop([0 0 0],[1,1,0],.01, ...
%%      linspace(-1,1,21),linspace(-1,1,21),linspace(-1,1,5))
%%%%%%%%%%%%%%%%%%%%%%%%%%%%%%%%%%%%%%%%%%%%%%%%%%%%%%%%%%%%%%%%%%%%%%%%

function [B_x,B_y,B_z]=unitcurrent_loop(center,d,radius,x,y,z);

d=d/norm(d); % normalized loop axis direction
mu_0 = pi*4e-7; % permeability of free space [m kg s^-2 A^-2]
B_0 = mu_0/2/radius; % field at center of loop, I=1.
[Xgrid,Ygrid,Zgrid] = meshgrid(x,y,z);
% Note: size(Xgrid)= (rows cols stacks), effectively swapping x&y
Xgrid=Xgrid-center(1); % offset center
Ygrid=Ygrid-center(2);
Zgrid=Zgrid-center(3);
%% H_grid: height of field point above the plane of the loop.
%% dot product of each field point with d vector
H_grid = d(1)*Xgrid + d(2)*Ygrid + d(3)*Zgrid;
%% R_x: x-coordinate of radial vector normal to loop axis toward
%% field point.
%% These R_ vectors are from the point of closest approach of the
%% loop axis to the field point.
R_X = Xgrid - d(1)*H_grid;
R_Y = Ygrid - d(2)*H_grid;
R_Z = Zgrid - d(3)*H_grid;
R_grid = sqrt(R_X.^2 + R_Y.^2 + R_Z.^2);
%% The operation above seems to cause a slight loss in precision,
%% resulting in tiny non-zero values where we should have
%% R_grid=0. We mark these and actual zeros by F, and replace
%% each resulting NaN with the corrected value.
F=find(R_grid<1e-10);
%% Field points within 1e-10 (0.1nm) of the loop axis are treated
%% as on-axis.
%% Normalize R_X,R_Y,R_Z and remove divide by zero points.
R_X = R_X./R_grid; R_X(F)=0;
R_Y = R_Y./R_grid; R_Y(F)=0;
R_Z = R_Z./R_grid; R_Z(F)=0;

```

```

%% Variables used to calculate field:
%% -----
%% alpha: scaled radial distance
%% beta: scaled axial distance
%% Q: function of alpha, beta. Always greater than 1
%% M: argument of the elliptic integral.
%% Matlab uses M=k^2 to compute the EI.
alpha = R_grid/radius;
beta = H_grid/radius;
Q = ((1+alpha).^2+beta.^2);
M = 4*alpha./Q; %
% warning off MATLAB:divideByZero;
gamma = H_grid./R_grid;
gamma(F)=0; %changes values NaN (divide by zero) to 0
tol = eps;
%% See help: 'ellipke' for explanation of elliptic integrals
[K,E] = ellipke(M,tol);
%% Radial field
B_R = (B_0/pi)*(gamma./sqrt(Q)).*(E.*(1 + alpha.^2 + beta.^2)./ ...
(Q-4*alpha)-K);
%% Axial field
B_H = (B_0/pi)*(1./sqrt(Q)).*(E.*(1 - alpha.^2 - beta.^2)./ ...
(Q-4*alpha)+K);
B_x = B_H*d(1) + B_R.*R_X;
B_y = B_H*d(2) + B_R.*R_Y;
B_z = B_H*d(3) + B_R.*R_Z;

```

A.3.2 Automatic Adwin script generation

A Matlab script 'Auto_coder.m' was written to print two Adwin-syntax include files: 'Auto_auto.aci', and 'Ext_auto.aci' which contain the set of conditionals, and required variable declarations respectively. The user input is limited to the variable names and their associated values. Together the output files allow automatic variable cycling, which can be activated at any time during the experiment by setting the external variable 'AUTO_ON' to 1 in the EV-GUI. A portion of 'Auto_coder.m' is shown:

```

%%%%%%%%%%
%% USER INPUT %%
%%%%%%%%%%
%% VARIABLE NAMES (MUST MATCH CORRESPONDING ADWIN NAMES)
AD_NAMES(1) = cellstr('T_NB');          %% V_{1}

```

```

AD_NAMES(2) = cellstr('I_NB_FINAL');    %% V_{2}
%% VARIABLE VALUES TO CYCLE
AD_NAMES{2,1} = [0 30 60]*1e6;          %%
AD_NAMES{2,2} = [0.285 0.29 0.295 0.3]; %%
%%%%%%%%%%%%%%%%%%%%%%%%%%%%%%%%%%%%%%%%%%%%%%%%%%%%%%%%%%%%%%%%%%%%%%%%
%% END OF USER INPUT %%
%%%%%%%%%%%%%%%%%%%%%%%%%%%%%%%%%%%%%%%%%%%%%%%%%%%%%%%%%%%%%%%%%%%%%%%%
%% Number of variables participating in Auto_mess
N = size(AD_NAMES,2);

%% OPEN (or create) the file 'Auto_auto.aci' with write privilege
fid = fopen('Auto_auto.aci', 'wt');
fprintf(fid, '#EXTERNAL AUTO_RUN_NUM\n');
fprintf(fid, 'AUTO_RUN_NUM = AUTO_RUN_NUM + 1\n');
fprintf(fid, '#INCLUDE [path]\\Modules\\Auto\\Ext_Auto.aci\n\n');
fprintf(fid, 'if(AUTO_RUN_NUM = 1)\n');
for n=1:N
    fprintf(fid, '\tVAR%g_---- = ', n);
    fprintf(fid, '%s', AD_NAMES{1,n}) ;
    fprintf(fid, '%g_%g\n', [n; size(AD_NAMES{2,n},2)]);
end
fprintf(fid, 'ENDIF\n\n');
for n=1:N
    fprintf(fid, 'IF(F%g_VAR%g= 1)\n', [n; n]);
    if n>1
        fprintf(fid, '\tF%g_VAR%g= 0\n', [n; n]);
    end
    for m=1:size(AD_NAMES{2,n},2)
        fprintf(fid, '\tIF(AND(VAR%g_---- = ', n);
        fprintf(fid, '%s', AD_NAMES{1,n}) ;
        fprintf(fid, '%g_%g;thr%g=0))\n', [n; m; n]);
        fprintf(fid, '\t\tVAR%g_---- = ', n);
        fprintf(fid, '%s', AD_NAMES{1,n}) ;
        fprintf(fid, '%g_%g\n', [n; 1+mod(m,size(AD_NAMES{2,n},2))]);
        fprintf(fid, '\t\tthr%g=1\n', n);
        if m==size(AD_NAMES{2,n},2) && n<N
            fprintf(fid, '\t\tF%g_VAR%g= 1\n', [n+1; n+1]);
        end
        fprintf(fid, '\tENDIF\n');
    end
end
end

```

```

        fprintf(fid, '\tthr%g=0\n', n);
        fprintf(fid, 'ENDIF\n\n');
    end
    for n=1:N
        fprintf(fid, '%s=VAR', AD_NAMES{1,n});
        fprintf(fid, '%g____\n', n);
    end
    % CLOSE the file 'Auto_auto.aci'
    fclose(fid);

```

The corresponding Adwin code written to the file 'Auto_auto.aci' is:

```

#EXTERNAL AUTO_RUN_NUM
AUTO_RUN_NUM = AUTO_RUN_NUM + 1
#include [path]\Modules\Auto\Ext_Auto.aci

if(AUTO_RUN_NUM = 1)
VAR1____ = T_NB1_3
VAR2____ = I_NB_FINAL2_4
ENDIF

IF(F1_VAR1= 1)
IF(AND(VAR1____ = T_NB1_1;thr1=0))
VAR1____ = T_NB1_2
thr1=1
ENDIF
IF(AND(VAR1____ = T_NB1_2;thr1=0))
VAR1____ = T_NB1_3
thr1=1
ENDIF
IF(AND(VAR1____ = T_NB1_3;thr1=0))
VAR1____ = T_NB1_1
thr1=1
F2_VAR2= 1
ENDIF
thr1=0
ENDIF

IF(F2_VAR2= 1)
F2_VAR2= 0
IF(AND(VAR2____ = I_NB_FINAL2_1;thr2=0))

```

```

VAR2_____ = I_NB_FINAL2_2
thr2=1
ENDIF
IF(AND(VAR2_____ = I_NB_FINAL2_2;thr2=0))
VAR2_____ = I_NB_FINAL2_3
thr2=1
ENDIF
IF(AND(VAR2_____ = I_NB_FINAL2_3;thr2=0))
VAR2_____ = I_NB_FINAL2_4
thr2=1
ENDIF
IF(AND(VAR2_____ = I_NB_FINAL2_4;thr2=0))
VAR2_____ = I_NB_FINAL2_1
thr2=1
ENDIF
thr2=0
ENDIF

T_NB=VAR1_____
I_NB_FINAL=VAR2_____

```

The same methods are used to produce the following code for 'Ext_auto.aci':

```

#EXTERNAL thr1=0
#EXTERNAL thr2=0

#EXTERNAL F1_VAR1=1
#EXTERNAL F2_VAR2=0

#EXTERNAL T_NB1_1 = 0.000
#EXTERNAL T_NB1_2 = 30000000.000
#EXTERNAL T_NB1_3 = 60000000.000

#EXTERNAL I_NB_FINAL2_1 = 0.285
#EXTERNAL I_NB_FINAL2_2 = 0.290
#EXTERNAL I_NB_FINAL2_3 = 0.295
#EXTERNAL I_NB_FINAL2_4 = 0.300

#EXTERNAL VAR1_____ = T_NB
#EXTERNAL VAR2_____ = I_NB_FINAL

```

```
#GLOBAL thr1=0
#GLOBAL thr2=0

#GLOBAL F1_VAR1=1
#GLOBAL F2_VAR2=0

#GLOBAL T_NB1_1 = 0.000
#GLOBAL T_NB1_2 = 30000000.000
#GLOBAL T_NB1_3 = 60000000.000

#GLOBAL I_NB_FINAL2_1 = 0.285
#GLOBAL I_NB_FINAL2_2 = 0.290
#GLOBAL I_NB_FINAL2_3 = 0.295
#GLOBAL I_NB_FINAL2_4 = 0.300

#GLOBAL VAR1_____ = T_NB
#GLOBAL VAR2_____ = I_NB_FINAL
// T_NB=VAR1_____
```

To see how the code works, let us consider a set of N variables labeled

$$\{V_1; V_2; \dots; V_n; \dots; V_N\} \quad (\text{A.1})$$

The variable values are denoted by

$$V_n = [V_{n,1}, V_{n,2}, \dots, V_{n,a}, \dots, V_{n,M_n}] \quad (\text{A.2})$$

where M_n is the number of values given for the n^{th} variable. As an example, let's imagine there are two variables. The cycling routine (a series of conditionals) increments to the next variable value, e.g. $V_{1,\alpha} \rightarrow V_{1,\alpha+1}$ at constant $V_{2,\beta}$. If $\alpha = M_n$, the following run begins by setting $V_1 = V_{1,1}$ and $V_2 = V_{2,\beta+1}$. The values of V_1 are then cycled again. This routine is easily extended to any number of variables. The total time for sampling every permutation once is given by $t_{run} \times \prod_{n=1}^N M_n$, where t_{run} is the duration of a single run. In the case printed above, for a single run time of $t_{run} = 1$ min, the total time required to cycle through the entire measurement would be $(3 \times 4) = 12$ min.

A.3.3 Data analysis GUI

The data analysis is streamlined by the use of a self-coded Matlab graphical user interface (GUI). This program, dubbed 'yoda', merges the 'proj_name.csv' file with set of measured values obtained from the processed absorption image, called 'param_set.mat'. While the 'proj_name.csv' file (also referred to as 'AWC_record') usually spans several weeks of

measurements, each day of measurements generates a new `'param_set'` that is stored along with absorption images in a folder named by the measurement date. The merging and subsequent filtering makes it possible to examine an arbitrary subset of the measurement. The results are plotted and organized to aid the subsequent analysis considerably. A screen shot of the yodaGUI is shown in Fig. A.4. Here we identify the three fields which take string inputs from top to bottom as:

- Date of measurement: (e.g. 21-Mar-2009).
- `'V_celler'` path. This file contains all user inputs, such as which variables to plot.
- `'AWC_record'` path. This file is a copy of `'proj_name.csv'`: the full ADwin record of global variables.

There are ten active buttons in the GUI. The three `'Browse *'` buttons open a dialog window (using the Matlab commands `'uigetfile'` or `'uigetdir'`) in order to actively retrieve file or folder paths. The two `'Open *'` buttons open the file at the specified path in the Matlab editor (using `'open'`) or default text editor (using `'winopen'`). The `'Create new V_celler'` button attempts to initialize a new user file (with the default required format), and opens the file in the Matlab editor. The action of the remaining buttons is summarized as follows:

- Up-date: attempts to access file `'proj_name.csv'` either on the master computer controlling ADwin, or from a local copy. It compares the file size with the currently used file and overwrites the local copy when the file sizes are different. The Up-date button only needs to be pressed when the data to analyze is newer than the locally stored `'AWC_record'` file.
- `'???'`: this button brings up a text box with some helpful usage tips.
- Initialize date: checks if there is an analysis folder for this date of measurements. If not, it creates one along with a default `'V_celler'`.
- Fertig: runs the routines for merging, filtering, and plotting the data.

Typically, one enters the date of measurement to be analyzed and presses `'initialize date'`. This automatically fills in a default `'V_celler'` path for this date. Once the correct path is given, along with the proper `'AWC_record'`, pressing `'Fertig'` begins the analysis, producing plots of the raw data which is output to the workspace in a set of dynamically named Matlab structs. An important point is that the program automatically detects the hard drive letter. What is more, all the entered information can be saved and loaded via the menu options. Usually this is unnecessary, since the program automatically stores the configuration of the last run and reloads it when yoda is re-called. Due to its length, it is not feasible to show the code here. Further documentation is available with the source code.

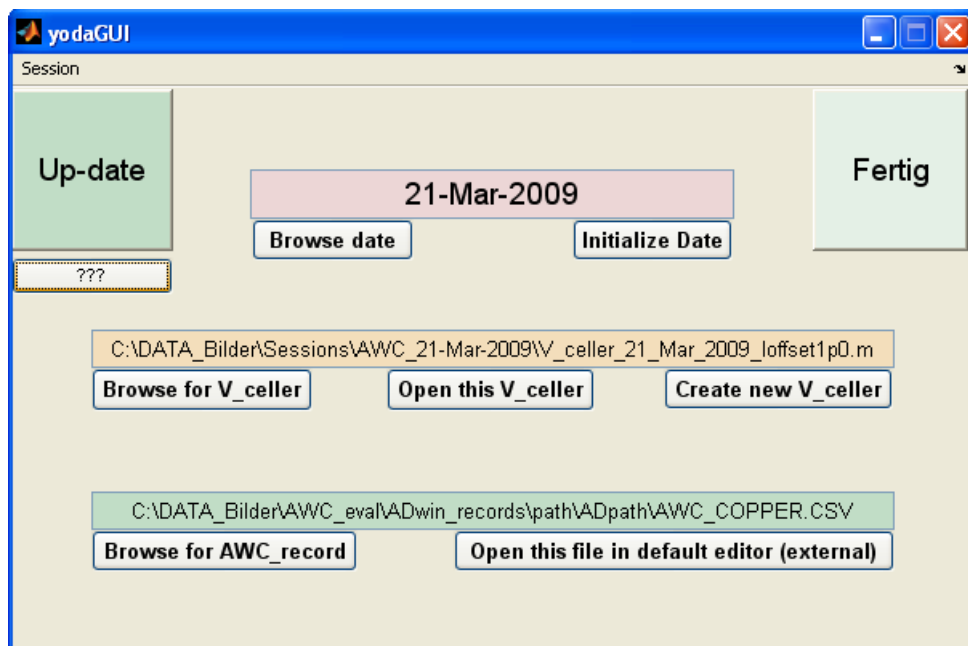


Figure A.4: Screen shot of yodaGUI.fig. The yodaGUI figure can be edited with the Matlab GUI helper 'guide'. Entering 'yoda' into the command line brings up the yodaGUI for streamlining measurement analysis.

Appendix B

Rubidium

B.1 Hyperfine structure

Fig. B.1 shows the rubidium fine and hyperfine structure for the 85 and 87 isotopes with natural abundances of 72.17% and 27.83%, respectively. This data is from D. Steck (Stea; Steb). An attempt has been made to draw portions of the spectrum to scale. Hyperfine splitting of the groundstate $5S_{1/2}$ level is roughly an order of magnitude larger than the hyperfine splitting of the excited P states, therefore the groundstate is scaled down by a factor of 10.

The hyperfine Hamiltonian in Alkali atoms has been discussed at length in (Ari77).

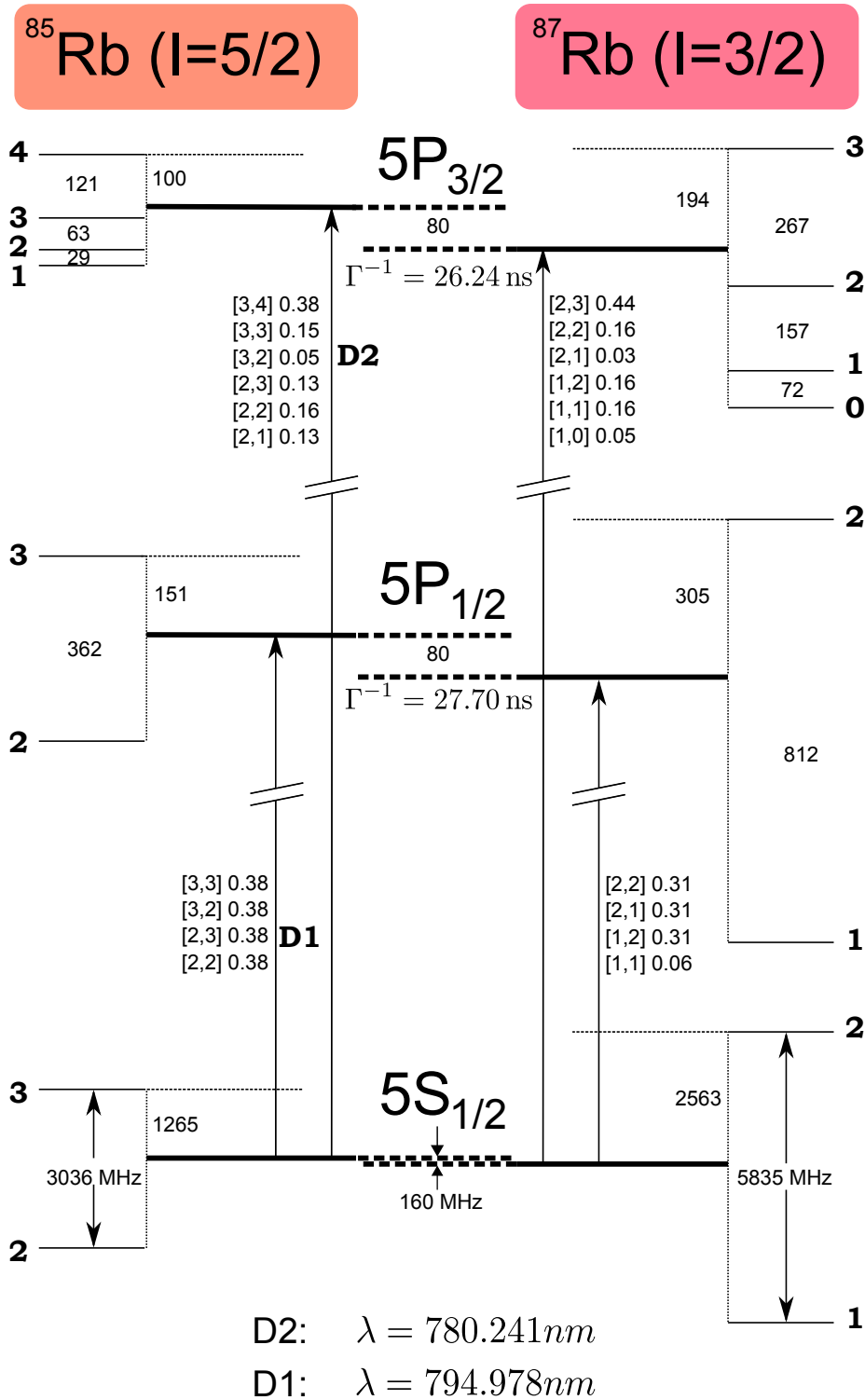


Figure B.1: Fine and hyperfine structure of the two most common rubidium ($Z = 37$) isotopes. The $5S_{1/2}$ groundstate has the largest hyperfine splitting (in the figure it is scaled by 1/10th with respect to the P levels).

Bibliography

- [Aga75a] G. S. Agarwal, *Quantum electrodynamics in the presence of dielectrics and conductors. I. Electromagnetic-field response functions and black-body fluctuations in finite geometries*, Phys. Rev. A **11**, 230 (1975).
- [Aga75b] G. S. Agarwal, *Quantum electrodynamics in the presence of dielectrics and conductors. II. Theory of dispersion forces*, Phys. Rev. A **11**, 243 (1975).
- [Ale03] A. S. Alexandrov, *Theory of Superconductivity: From Weak to Strong Coupling*, (Institute of Physics, Bristol, 2003).
- [Ari77] E. Arimondo, M. Inguscio and P. Violino, *Experimental determinations of the hyperfine structure in the alkali atoms*, Rev. Mod. Phys. **49**, 31 (1977).
- [Bar57] J. Bardeen, L. N. Cooper and J. R. Schrieffer, *Theory of Superconductivity*, Phys. Rev. **108**, 1175 (1957).
- [Bri06] D. M. Brink and C. V. Sukumar, *Majorana spin-flip transitions in a magnetic trap*, Phys. Rev. A **74**, 035401 (2006).
- [Buc04] Werner Buckel and Reinhold Kleiner, *Superconductivity*, (Wiley-VCH, 2004).
- [Byr92] Frederick W Byron and Robert W Fuller, *Mathematics of Classical and Quantum Physics*, (Dover Publications, New York, 1992).
- [Can08a] D. Cano, B. Kasch, H. Hattermann, R. Kleiner, C. Zimmermann, D. Koelle and J. Fortágh, *Meissner Effect in Superconducting Microtraps*, Phys. Rev. Lett. **101**, 183006 (2008).
- [Can08b] D. Cano, B. Kasch, H. Hattermann, D. Koelle, R. Kleiner, C. Zimmermann and J. Fortágh, *Impact of the Meissner effect on magnetic microtraps for neutral atoms near superconducting thin films*, Phys. Rev. A **77**, 063408 (2008).
- [Can09] Daniel Cano, *Meissner effect in superconducting microtraps*, PhD thesis Eberhard-Karls-Universität Tübingen 2009.
- [Cas98] Y. Castin, J. I. Cirac and M. Lewenstein, *Reabsorption of Light by Trapped Atoms*, Phys. Rev. Lett. **80**, 5305 (1998).

- [Cas05] S. Casalbuoni, E.A. Knabbe, J. Kötzler, L. Lilje, L. von Sawilski, P. Schmüser and B. Steffen, *Surface superconductivity in niobium for superconducting RF cavities*, Nucl. Instrum. Methods Phys. Res., Sect. A **538**, 45 (2005).
- [Cha03] Lawrie Challis and Fred Sheard, *The Green of Green Functions*, Phys. Today **56**, 41 (2003).
- [Cou98] Ph. Courteille, R. S. Freeland, D. J. Heinzen, F. A. van Abeelen and B. J. Verhaar, *Observation of a Feshbach Resonance in Cold Atom Scattering*, Phys. Rev. Lett. **81**, 69 (1998).
- [Dal89] J. Dalibard and C. Cohen-Tannoudji, *Laser cooling below the Doppler limit by polarization gradients: simple theoretical models*, J. Opt. Soc. Am. B: Opt. Phys. **6**, 2023 (1989).
- [Dik09] V. Dikovskiy, V. Sokolovskiy, B. Zhang, C. Henkel and R. Folman, *Superconducting atom chips: advantages and challenges*, Eur. Phys. J. D **51**, 13 pages (2009).
- [Dun98] Ho Trung Dung, Ludwig Knöll and Dirk-Gunnar Welsch, *Three-dimensional quantization of the electromagnetic field in dispersive and absorbing inhomogeneous dielectrics*, Phys. Rev. A **57**, 3931 (1998).
- [E.D] J.P. Le E.D. Marquardt and Ray Radebaugh, *Cryogenic Material Properties Database*, Presented at the 11th International Cryocooler Conference June 20-22, 2000 Keystone, Co.
- [Emm09] Andreas Emmert, Adrian Lupascu, Gilles Nogues, Michel Brune, Jean-Michel Raimond and Serge Haroche, *Measurement of the trapping lifetime close to a cold metallic surface on a cryogenic atom-chip*, 0901.4331 (2009).
- [Es09] J. J. P van Es, P. Wicke, A. H van Amerongen, C. Rétif, S. Whitlock and N. J van Druuten, *Box traps on an atom chip for one-dimensional quantum gases*, 0911.5250 (2009).
- [Ess67] U. Essmann and H. Träuble, *The direct observation of individual flux lines in type II superconductors*, Physics Lett. A **24**, 526 (1967).
- [Fer06] R. Fermani, S. Scheel and P. L. Knight, *Spatial decoherence near metallic surfaces*, Phys. Rev. A **73**, 032902 (2006).
- [Fey82] Richard Feynman, *Simulating physics with computers*, International Journal of Theoretical Physics **21**, 467 (1982).
- [For07] József Fortágh and Claus Zimmermann, *Magnetic microtraps for ultracold atoms*, Rev.s of Modern Physics **79**, 235 (2007).

- [Fri00] Jonathan R. Friedman, Vijay Patel, W. Chen, S. K. Tolpygo and J. E. Lukens, *Quantum superposition of distinct macroscopic states*, Nature **406**, 43 (2000).
- [Geh98] M. E. Gehm, K. M. O'Hara, T. A. Savard and J. E. Thomas, *Dynamics of noise-induced heating in atom traps*, Phys. Rev. A **58**, 3914 (1998).
- [Gin50] V. L Ginzburg and L. D Landau, *On the Theory of superconductivity*, Zh. Eksp. Teor. Fiz. **20**, 1064 (1950).
- [Gri99] Rudolf Grimm, Matthias Weidemüller and Yurii B Ovchinnikov, *Optical dipole traps for neutral atoms*, physics/9902072 (1999).
- [Gru96] T. Gruner and D.-G. Welsch, *Green-function approach to the radiation-field quantization for homogeneous and inhomogeneous Kramers-Kronig dielectrics*, Phys. Rev. A **53**, 1818 (1996).
- [Gün07] A. Günther, S. Kraft, C. Zimmermann and J. Fortágh, *Atom Interferometer Based on Phase Coherent Splitting of Bose-Einstein Condensates with an Integrated Magnetic Grating*, Physical Review Letters **98** (2007).
- [Hän01] W. Hänsel, P. Hommelhoff, T. W. Hänsch and J. Reichel, *Bose-Einstein condensation on a microelectronic chip*, Nature **413**, 498 (2001).
- [Har03] D. M Harber, J. M McGuirk, J. M Obrecht and E. A Cornell, *Thermally Induced Losses in Ultra-Cold Atoms Magnetically Trapped Near Room-Temperature Surfaces*, cond-mat/0307546 (2003).
- [Hec98] Eugene Hecht, *Optics*, (Addison Wesley, 1998) 3 edition.
- [Hen99] C. Henkel, S. Pötting and M. Wilkens, *Loss and heating of particles in small and noisy traps*, Applied Physics B: Lasers and Optics **69**, 379 (1999).
- [Hen05] C. Henkel, *Magnetostatic field noise near metallic surfaces*, Eur. Phys. J. D - Atomic, Molecular, Optical and Plasma Physics **35**, 59 (2005).
- [Hoh07] Ulrich Hohenester, Asier Eiguren, Stefan Scheel and E. A. Hinds, *Spin-flip lifetimes in superconducting atom chips: Bardeen-Cooper-Schrieffer versus Eliashberg theory*, Phys. Rev. A **76**, 033618 (2007).
- [Huf09] Christoph Hufnagel, Tetsuya Mukai and Fujio Shimizu, *Stability of a superconductive atom chip with persistent current*, Phys. Rev. A **79**, 053641 (2009).
- [Jon03] M. P. A. Jones, C. J. Vale, D. Sahagun, B. V. Hall and E. A. Hinds, *Spin Coupling between Cold Atoms and the Thermal Fluctuations of a Metal Surface*, Phys. Rev. Lett. **91**, 080401 (2003).

- [Kas10] B. Kasch, H. Hattermann, D. Cano, T. E Judd, S. Scheel, C. Zimmermann, R. Kleiner, D. Koelle and J. Fortágh, *Cold atoms near superconductors: Atomic spin coherence beyond the Johnson noise limit*, New J. Phys. 12 065024 (2010) ArXiv: 0906.1369.
- [Kat99] Hidetoshi Katori, Tetsuya Ido, Yoshitomo Isoya and Makoto Kuwata-Gonokami, *Magneto-Optical Trapping and Cooling of Strontium Atoms down to the Photon Recoil Temperature*, Phys. Rev. Lett. **82**, 1116 (1999).
- [Lan10] B. P. Lanyon, J. D. Whitfield, G. G. Gillett, M. E. Goggin, M. P. Almeida, I. Kassal, J. D. Biamonte, M. Mohseni, B. J. Powell, M. Barbieri, A. Aspuru-Guzik and A. G. White, *Towards quantum chemistry on a quantum computer*, Nature Chemistry (2010).
- [Let88] Paul D. Lett, Richard N. Watts, Christoph I. Westbrook, William D. Phillips, Phillip L. Gould and Harold J. Metcalf, *Observation of Atoms Laser Cooled below the Doppler Limit*, Phys. Rev. Lett. **61**, 169 (1988).
- [Lon38] F. London, *The lambda phenomenon of Liquid Helium and the Bose-Einstein degeneracy*, Nature **141**, 643 (1938).
- [Lui96] O. J. Luiten, M. W. Reynolds and J. T. M. Walraven, *Kinetic theory of the evaporative cooling of a trapped gas*, Phys. Rev. A **53**, 381 (1996).
- [Mue08] T. Mueller, X. Wu, A. Mohan, A. Eyvazov, Y. Wu and R. Dumke, *Towards a guided atom interferometer based on a superconducting atom chip*, 0806.1789 (2008).
- [Muk07] T. Mukai, C. Hufnagel, A. Kasper, T. Meno, A. Tsukada, K. Semba and F. Shimizu, *Persistent Supercurrent Atom Chip*, Phys. Rev. Lett. **98**, 260407 (2007).
- [nas] *Outgassing Data for Selecting Spacecraft Materials System*, <http://outgassing.nasa.gov/>.
- [Nie00] Michael A. Nielsen and Isaac L. Chuang, *Quantum computation and quantum information*, (Cambridge University Press, 2000).
- [O'H03] John F. O'Hanlon, *A User's Guide to Vacuum Technology*, (Wiley-Interscience, 2003) 3 edition.
- [Ott01] H. Ott, J. Fortágh, G. Schlotterbeck, A. Grossmann and C. Zimmermann, *Bose-Einstein Condensation in a Surface Microtrap*, Phys. Rev. Lett. **87**, 230401 (2001).
- [Pet08] David Petrosyan and Michael Fleischhauer, *Quantum Information Processing with Single Photons and Atomic Ensembles in Microwave Coplanar Waveguide Resonators*, Phys. Rev. Lett. **100**, 170501 (2008).

- [Pet09] David Petrosyan, Guy Bensky, Gershon Kurizki, Igor Mazets, Johannes Majer and Jorg Schmiedmayer, *Reversible state transfer between superconducting qubits and atomic ensembles*, Phys. Rev. A **79**, 040304 (2009).
- [Pip53] A. B. Pippard, *An Experimental and Theoretical Study of the Relation between Magnetic Field and Current in a Superconductor*, Royal Society of London Proceedings Series A **216**, 547 (1953).
- [Raa87] E. L. Raab, M. Prentiss, Alex Cable, Steven Chu and D. E. Pritchard, *Trapping of Neutral Sodium Atoms with Radiation Pressure*, Phys. Rev. Lett. **59**, 2631 (1987).
- [Rek04] P. K. Rekdal, S. Scheel, P. L. Knight and E. A. Hinds, *Thermal spin flips in atom chips*, Phys. Rev. A **70**, 013811 (2004).
- [Ric95] L. Ricci, *A compact grating-stabilized diode laser system for atomic physics*, Optics Communications **117**, 541 (1995).
- [Rou08] C. Roux, A. Emmert, A. Lupascu, T. Nirrengarten, G. Nogues, M. Brune, J.-M. Raimond and S. Haroche, *Bose-Einstein condensation on a superconducting atom chip*, EPL (Europhysics Lett.) **81**, 56004 (2008).
- [Sav97] T. A. Savard, K. M. O'Hara and J. E. Thomas, *Laser-noise-induced heating in far-off resonance optical traps*, Phys. Rev. A **56**, R1095 (1997).
- [Sch98] Stefan Scheel, Ludwig Knöll and Dirk-Gunnar Welsch, *QED commutation relations for inhomogeneous Kramers-Kronig dielectrics*, Phys. Rev. A **58**, 700 (1998).
- [Sch99] S. Scheel, L. Knöll and D.-G. Welsch, *Spontaneous decay of an excited atom in an absorbing dielectric*, Phys. Rev. A **60**, 4094 (1999).
- [Sch03] E. Schachinger and J.P. Carbotte, *Extended Eliashberg Theory for d-Wave Superconductivity and Application to Cuprates*, Review article, J. Phys. Stud. **7**, 209 (2003).
- [Sch05] S. Scheel, P. K. Rekdal, P. L. Knight and E. A. Hinds, *Atomic spin decoherence near conducting and superconducting films*, Phys. Rev. A **72**, 042901 (2005).
- [Sch07] Stefan Scheel, Rachele Fermani and E. A. Hinds, *Feasibility of studying vortex noise in two-dimensional superconductors with cold atoms*, Phys. Rev. A **75**, 064901 (2007).
- [She89] Y. Shevy, D. S. Weiss, P. J. Ungar and Steven Chu, *Bimodal speed distributions in laser-cooled atoms*, Phys. Rev. Lett. **62**, 1118 (1989).

- [Shi09] Fujio Shimizu, Christoph Hufnagel and Tetsuya Mukai, *Stable Neutral Atom Trap with a Thin Superconducting Disc*, Physical Review Letters **103** (2009).
- [Sho95] Peter Shor, *Scheme for reducing decoherence in quantum computer memory*, Physical Review A **52**, R2493 (1995).
- [Sin09] Mandip Singh, *Macroscopic entanglement between a Bose Einstein condensate and a superconducting loop*, Opt. Express **17**, 2600 (2009).
- [Ska06] Bo-Sture K. Skagerstam, Ulrich Hohenester, Asier Eiguren and Per Kristian Rekdal, *Spin Decoherence in Superconducting Atom Chips*, Phys. Rev. Lett. **97**, 070401 (2006).
- [Sør04] Anders S. Sørensen, Caspar H. van der Wal, Lilian I. Childress and Mikhail D. Lukin, *Capacitive Coupling of Atomic Systems to Mesoscopic Conductors*, Phys. Rev. Lett. **92**, 063601 (2004).
- [Stea] Daniel A. Steck, *Rubidium 85 D Line Data*,.
- [Steb] Daniel A. Steck, *Rubidium 87 D Line Data*,.
- [Tow95] C. G. Townsend, N. H. Edwards, C. J. Cooper, K. P. Zetie, C. J. Foot, A. M. Steane, P. Szriftgiser, H. Perrin and J. Dalibard, *Phase-space density in the magneto-optical trap*, Phys. Rev. A **52**, 1423 (1995).
- [Vog06] Werner Vogel, Dirk-Gunnar Welsch and Sascha Wallentowitz, *Quantum optics*, (Wiley-VCH, 2006).
- [Wal00] Caspar H. van der Wal, A. C. J. ter Haar, F. K. Wilhelm, R. N. Schouten, C. J. P. M. Harmans, T. P. Orlando, Seth Lloyd and J. E. Mooij, *Quantum Superposition of Macroscopic Persistent-Current States*, Science **290**, 773 (2000).
- [Web69] G. W. Webb, *Low-Temperature Electrical Resistivity of Pure Niobium*, Phys. Rev. **181**, 1127 (1969).
- [Wei03a] Matthias Weidemüller and Claus Zimmermann, *Interactions in ultracold gases*, (Wiley-VCH, 2003).
- [Wei03b] John Weiner, *Cold and Ultracold Collisions in Quantum Microscopic and Mesoscopic Systems*, (Cambridge University Press, Cambridge, UK, 2003).
- [Zur03] Wojciech H Zurek, *Decoherence and the transition from quantum to classical – REVISITED*, quant-ph/0306072 (2003).

Hiermit erkläre ich, dass ich diese Arbeit selbst verfasst und keine anderen als die angegebenen Quellen und Hilfsmittel benutzt habe.

Urbana-Champaign, den 9. März 2010 _____